# UNIVERSIDAD DE INVESTIGACIÓN DE TECNOLOGÍA EXPERIMENTAL YACHAY

## Escuela de Ciencias Físicas y Nanotecnología

## TÍTULO: Modeling electronic properties of polymeric-based composite thin films

Trabajo de integración curricular presentado como requisito para la obtención del título de Físico.

**Autor:**

Macharé Gallardo Juan José

**Tutor:**

Duncan J. Mowbray, PhD.

Urcuquí, febrero 2023

# AUTORÍA

Yo, **Juan José Macharé Gallardo**, con cédula de identidad 0706262763, declaro que las ideas, juicios, valoraciones, interpretaciones, consultas bibliográficas, definiciones y conceptualizaciones expuestas en el presente trabajo; así cómo, los procedimientos y herramientas utilizadas en la investigación, son de absoluta responsabilidad de el/la autora (a) del trabajo de integración curricular. Así mismo, me acojo a los reglamentos internos de la Universidad de Investigación de Tecnología Experimental Yachay.

Urcuquí, febrero 2023.

<div align="center">

_____

Juan José Macharé Gallardo
CI: 0706262763

</div>

# AUTORIZACIÓN DE PUBLICACIÓN

Yo, **Juan José Macharé Gallardo**, con cédula de identidad 0706262763, cedo a la Universidad de Investigación de Tecnología Experimental Yachay, los derechos de publicación de la presente obra, sin que deba haber un reconocimiento económico por este concepto. Declaro además que el texto del presente trabajo de titulación no podrá ser cedido a ninguna empresa editorial para su publicación u otros fines, sin contar previamente con la autorización escrita de la Universidad.

Asimismo, autorizo a la Universidad que realice la digitalización y publicación de este trabajo de integración curricular en el repositorio virtual, de conformidad a lo dispuesto en el Art. 144 de la Ley Orgánica de Educación Superior

Urcuquí, febrero 2023.

<div style="text-align:center">

———————————————

Juan José Macharé Gallardo
CI: 0706262763

</div>

# Dedicatoria

A mi madre Graciela Gallardo, porque este logro es gracias a usted.

*Juan*

# Agradecimiento

A mis padres Alberto y Graciela, por todo el apoyo recibido en mi vida. A mis hermanos Leonidas y Renata. A mi novia Anita. Gracias por todo su apoyo.

Thanks to Professor Duncan Mowbray for all the support and everything that I learned together with him.

*Juan*

# Resumen

Las películas delgadas de compuestos de base polimérica han sido muy estudiadas en las últimas décadas debido a sus múltiples aplicaciones. Esto se debe a que son materiales que presentan las propiedades físico-químicas tanto del compuesto polimérico como del nanomaterial con el que se fabrica el composito (eléctricas, mecánicas y térmicas). Por esta razón, el modelado de estas propiedades de los CPC es una parte fundamental para predecir su comportamiento como material. En esta tesis se desarrolla un método ab initio para modelar la conductividad anisotrópica de un CPC estirado hecho de una matriz polimérica de alcohol polivinílico (PVA) mezclado con nanotubos de carbono de pared simple (SWCNTs). Estas cantidades se obtienen mediante una combinación de cálculos de teoría funcional de la densidad, métodos basados en la función de Green de no equilibrio y un modelo estadístico geométrico de deformación afín. De este modo, proporcionamos una descripción cualitativa y semicuantitativa de la conductividad anisotrópica medida de las CPC de PVA/SWCNT. El éxito de este modelo demuestra que la conductividad de los CPCs viene determinada por (1) la conectividad de la red de SWCNTs dentro de la matriz polimérica, (2) la resistencia al salto de la conductancia intertubular, (3) la concentración de SWCNTs en la muestra, y (4) la cantidad de estiramiento y el parámetro de orden orientacional concomitante de los SWCNTs en el compuesto. El modelo desarrollado puede aplicarse potencialmente para obtener CPCs con una conductividad anisotrópica deseada basados en nanomateriales conductores balísticos, es decir, SWCNTs, y diferentes matrices poliméricas.

**Palabras Clave:** nanocomposito, teroría de la densidad funcional (DFT), conductividad anisotrópica, métodos de Monte Carlo, nanotubos de carbono de pared simple (SWCNTs).

# Abstract

Thin films of polymer-based composites have been widely studied in recent decades due to their multiple applications. This is because they are materials that exhibit the physicochemical properties of both the polymer composite and the nanomaterial from which the composite is made (electrical, mechanical and thermal). For this reason, modeling these properties of CPCs is a fundamental part of predicting their behavior as a material. In this thesis, an ab initio method is developed to model the anisotropic conductivity of a stretched CPC made of a polymeric matrix of polyvinyl alcohol (PVA) mixed with single-walled carbon nanotubes (SWCNTs). These quantities are obtained by a combination of density functional theory calculations, non-equilibrium Green's functions based methods and an affine deformation geometric statistical statistical model. In this way, we provide a qualitative and semi-quantitative description of the measured anisotropic conductivity of PVA/SWCNT CPCs. The success of this model demonstrates that the conductivity of CPCs is determined by (1) the connectivity of the SWCNTs network within the polymer matrix, (2) the resistance to intertubular conductance hopping, (3) the concentration of SWCNTs in the sample, and (4) the amount of stretching and the concomitant orientational order parameter of the SWCNTs in the composite. The developed model can potentially be applied to obtain CPCs with desired anisotropic conductivity based on ballistic conductive nanomaterials, i.e., SWCNTs, and different polymeric matrices.

**Keywords:** nanocomposite, density functional theory (DFT), anisotropic conductivity, Monte Carlo methods, SWCNTs

# Contents

# List of Figures

# List of Tables

# Chapter 1

# Introduction

The advancement of technology has led to a competition to find the best instruments and components for more significant social development. This involves the study of various materials to report their behavior when subjected to different conditions, leading to significant improvements in the understanding of materials in recent decades. Some of the most interesting materials are industrially scalable conductive polymer-based composites (CPCs). These are usually manufactured by combining a polymer matrix together with a conductive nanomaterial. In this way, one may provide polymers, typically non-conductive materials, with properties of the nanomaterial, such as improved electrical conductivity. Conductive polymers have been widely investigated and used in applications such as solar cells, transistors, thermo-electric power-generation, microwave absorption, electrochromic devices, photo-current generation, supercapacitors, and light emitting diodes[1].

The development of these types of conductive polymers can be carried out with different materials that provide the CPC with an improved conductivity. Some materials commonly used to improve the conductivity of polymers are metallic materials, nano-particles, and carbon-based nano-materials such as graphene, and carbon nanotubes (CNTs). The latter has been perhaps the most interesting candidate material since it was found in transmission electron microscopy (TEM) images by Sumio Iijima in 1991[2]. Specifically, CNTs have led to a long line of research on CPC materials based on their high tensile strength, thermal conductivity, and tailorable electronic properties.[3] This has resulted in a great interest in the potential application of CNTs

in a diverse range of areas including biology, medicine, technology, and materials science. The most common applications for CNTs range from electronics as transistors[4,5] to medicine as a drug delivery mechanism for treating diseases[2]. The interesting properties of CNTs (high tensile strength, ballistic conduction, metallicity or semiconductivity, etc.)[4] have led researchers to try to functionalize CNTs with other materials. One of the functionalization fields that has been most studied and used is embedding CNTs within polymeric thin films[6]. When preparing polymeric films with CNTs, the embedded CNTs share their mechanical, thermal, and electronic properties with the polymer, resulting in a composite material with tailorable conductive properties and improved mechanical resistance.

Carbon nanotubes can be divided into two main types: single-walled carbon nanotubes (SWCNTs) and multi-walled carbon nanotubes (MWCNTs). SWCNTs can be imagined as a (2D) graphene sheet that has been rolled into the shape of a cylinder, whereas MWCNTs consist of several graphene sheets rolled into a series of concentric cylinders with a common axis. In each case, the atomic structure of each layer is determined by the chirality of the tube. This is defined by the chiral vector $\mathbf{C}_h$, which traces out the tube's circumference on the graphene surface. The chiral vector $\mathbf{C}_h$ can be expressed in terms of graphene's primitive unit vectors $\mathbf{a}_1$ and $\mathbf{a}_2$ as

$$\mathbf{C}_h \equiv n\mathbf{a}_1 + m\mathbf{a}_2 \qquad (1.1)$$

where $n, m \in \mathbb{Z}^+$ denotes the chirality of the tube. These properties may be further categorized using the chiral angle $\theta$ between the so-called "zigzag" or $(n, 0)$ and "armchair" or $(n, n)$ nonchiral directions on the graphene surface, as shown in Figure 1.1[7]. Specifically, SWCNTs with $n - m = 0$ mod 3 are metallic, whereas SWCNTs with $n - m \neq 0$ are semiconducting.[3,8–10]

Applications of anisotropically conductive materials based on ordered SWCNTs in electronics and optoelectronics include waveguides, optical communication, sensors, photoelectric imaging, polarization-sensitive detectors, and developing shape memory composites[11]. Typically, the manufacture of the latter materials ranges from the use of filtration under vacuum or high pressure, fiber drawing/spinning, employing magnetic/electric field, compression, to mechanical shearing or stretching, i.e., hot-drawing.[12–16]. All of these techniques exhibit their own advantages and disadvantages depending on the final intended use. However, among them, mechanical stretching deserves special attention for the fabrication of anisotropic free-standing films based on SWCNTs due to its facile implementation and associated cost-effectiveness. Moreover, it allows one to
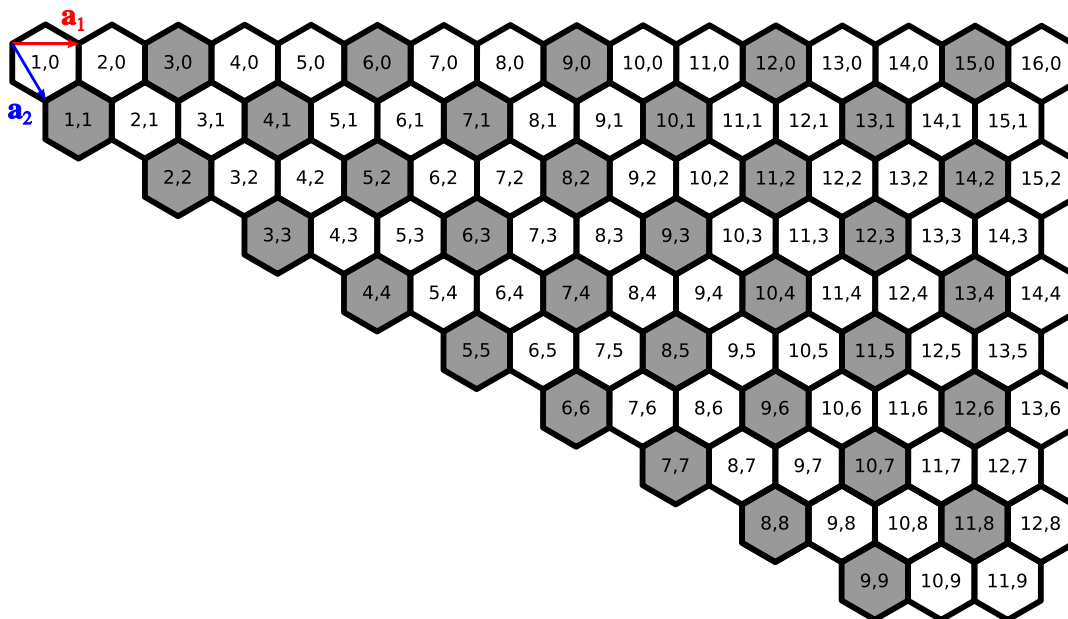
Figure 1.1: SWCNT indices $(n, m)$ of chiral or circumference vector $\mathbf{C}_h \equiv n\mathbf{a}_1 + n\mathbf{a}_2$ where $\mathbf{a}_1$ (red) and $\mathbf{a}_2$ (blue) are unit vectors of graphene's sheet. Metallic SWCNT chiralities ($n - m \equiv 0$ mod 3) are marked in grey, whereas semiconducting SWCNT chiralities ($n - m \neq 0$ mod 3) are marked in white .

control the orientational order parameter of the SWCNTs within the composite and, in this way, control their concomitant electronic/mechanical properties[14–16].

Technological advances in the synthesis of CPCs with various polymer and conductive additive molecules open even more possibilities within the composite manufacturing industry. The final performance of such materials will dramatically depend on both the homogenous distribution of the conductive additive within the composite and their spatial ordering[12,17–19]. For instance, an inadequate distribution of the additive throughout the material would negatively impact their mechanical or electronic performance within the CPC[20]. In ceramics, or composites materials in general, agglomeration of particles often induces mechanical concentration stresses. making them more fragile structures[21]. Orientational ordering is especially important for functional materials and biological tissues in which a certain order through a preferential direction is necessary to accomplish their desired function[13,15,22]. In fact, many biological examples illustrate

how an oriented structure can enhance the response to external stimulii [13,22–24]. Anisotropies are often crucial for electronic properties such as heat or electrical transport so that a more or less well-aligned percolation path is required in order to permit transport [12,14–16]. Conductive additives include, but are not limited to, planar/lamellar/layered-like, fiber-like, and rod-like structures [12,14,16,17,25–27]. In this context, SWCNTs have been demonstrated to be very suitable for these types of applications [14,15,28–30].

Despite the first works related to the development of orderly SWCNT arrays with enhanced electrical properties appearing almost 20 years ago, several open questions remain regarding the effective mechanism involved during electronic transport. Besides this, the typical processing drawbacks associated with finding a cost-efficient route to control both the homogeneous incorporation of SWCNTs in polymeric matrices and their anisotropies may hinder the resulting CPC's electronic response and potential applications [12,17,31,32].

To obtain a clearer idea of what happens in a polymer/SWCNT composite, a theoretical model is needed which will allow us to interpret what occurs at a mechanistic level within the CPC. The most used method to carry out these types of studies is density functional theory (DFT). DFT uses the electron density distribution to describe the ground state energy and electronic structure of a system and simulate its quantum mechanical properties. Using a DFT-based spatially localized hamiltonian for the system and non-equilibrium Green's functions methods, one may describe the scattering processes during electronic transport, and thus the intertube conductance between phyisorbed SWCNTs. Through the use of computational power, DFT and NEGF methods have allowed properties of novel materials to be predicted, permitting the design of a material without wasting time, energy, materials and budget synthesizing less-than promising candidate materials [33,34].

## 1.1 Problem Statement

This thesis aims to define an efficient and accurate method based on DFT calculations to characterize materials theoretically and establish a general model to describe qualitatively and semiquantitatively the conductivity of a thin film polymeric composite with a carbon-based nanomaterial, that is, SWCNTs. To do so, we have used the Python programming language together with the

GPAW module to perform DFT calculations, which is based on the projector-augmented wave (PAW) method, together with the atomic simulation environment (ASE) in which we can generate the molecular species to be used in the system. All computational details are specified in the methodology section.

## 1.2 General and Specific Objectives

The objective of this thesis is to establish a general theoretical model to calculate how conductivity changes as a function of concentration and extension ratio $\lambda$, *via* comparison with values obtained experimentally from a polymer/CNT composite. The study of this system will allow us to establish at which concentrations we can obtain a significant increase in the anisotropic conductivity of a composite as we increase the extension ratio parameter. Atomic units ($\hbar = e = m_e = 4\pi\epsilon_0 = a_0 = 1$) have been used throughout unless stated otherwise.

## 1.3 Overview

The present work is composed of five chapters and appendices, with Chapter 1 introducing the overall problem, establishing the methods we will employ to solve it, and expressing the objectives of this thesis. Chapter 2 focuses on explaining the theoretical basis behind the methodology used in this research, through the density functional theory, percolation theory, and random walk systems.. Chapter 3 explains the methodology used to perform our DFT calculations, the model to find the conductivity of the composite, and all necessary computational details for their reproduction. Chapter 4 discusses the results of our calculations and the obtaimed model obtained in order to specify which methods bore fruit in reproducing the measured anisotropic conductivity of hot-drawn PVA/SWCNT CPCs. Finally, in Chapter 5, the conclusions of this thesis are established and suggestions for future studies based on similar composites are provided.

# Chapter 2

# Theoretical Background

## 2.1   The Many Body Problem

In general, physical systems are described by their associated Hamiltonian $\hat{\mathcal{H}}$ and quantum systems are no exception. One of the most simple quantum systems is the isolated hydrogen atom, which can be solved analytically. However, to solve systems involving molecules one must also consider the complexity of the calculations because they are by definition many-body problems.

The many-body time-dependent wave function $\Psi$ of a quantum system is the solution to the time-dependent Schrödinger equation

$$i\hbar\frac{\partial}{\partial t}\Psi = \hat{\mathcal{H}}\Psi, \tag{2.1}$$

which is generally a linear partial differential equation.[35] All physical observables of the system may be deduced from the eigenfunctions and eigenvalues of (2.1). For a generic molecular system, its ground state hamiltonian may be expressed as

$$\hat{\mathcal{H}} = \hat{T}_e + V_{e-n} + V_{e-e} + \hat{T}_n + V_{n-n}. \tag{2.2}$$

Each term in (2.2) represents a different interaction that occurs in the physical system. The first term represents the kinetic energy of the electrons, $\hat{T}_e$, the second represent the Coulomb

interaction potential between oppositely charged particles in the nucleus and its surroundings., $V_{e-n}$, the third represent the repulsive potential that exists between electrons, $V_{e-e}$, the fourth represent the kinetic energy for nuclei, $\hat{T}_n$, and, finally, the last term represent the repulsive potential that exist between nuclei, $V_{n-n}$.

In this way the Hamiltonian operator $\hat{\mathcal{H}}$ of (2.2) is a linear differential operator, which acts on the wavefunction $\Psi$ in space and time. Since the potentials in (2.7) only depend on position but not time, $\Psi$ is separable into a time-dependent part $\tau(t)$ and a time-independent part $\Psi$, with their eigenvalue $E_{\text{tot}}$ being the system's total energy. Considering this information, time-independent Schrödinger equation can be expressed as

$$\hat{\mathcal{H}}\Psi = E_{\text{tot}}\Psi. \tag{2.3}$$

Notice that we define the wavefunction as $\Psi$ and not $\Psi$ because this is a part of the total wave function which only contains the positional information of the total wavefunction $\Psi$. This means the general solution to (2.1) is a linear combination of all eigenfunctions $\Psi_n$ and eigenvalues $E_n$ of (2.3), so that

$$\Psi = \sum_{n=0}^{\infty} C_n \Psi_n e^{-\iota E_n t/\hbar}. \tag{2.4}$$

The solutions of (2.3) may be defined in terms of the positions and spins of the system's $n_e$ electrons and $N_n$ nuclei as

$$\Psi(\mathbf{r}_1, s_1, ..., \mathbf{r}_{n_e}, s_{n_e}; \mathbf{R}_1, S_1, ..., \mathbf{R}_{N_n}, S_{N_n}), \tag{2.5}$$

where $\mathbf{r}_i$ and $s_i$ are the coordinates and spin of the $i^{\text{th}}$ electron, and $\mathbf{R}_I$ and $S_I$ are the coordinates and spin of the $I^{\text{th}}$ nuclei. Employing atomic units ($\hbar = e = m_e = a_0 = 1$), the many-body Hamiltonian operator, $\hat{\mathcal{H}}$, of (2.2) is then

$$\hat{\mathcal{H}} = -\frac{1}{2}\sum_{i=1}^{n_e}\nabla_{\mathbf{r}_i}^2 - \sum_{i=1}^{n_e}\sum_{I=1}^{N_n}\frac{Z_I}{|\mathbf{r}_i - \mathbf{R}_I|} + \sum_{i=1}^{n_e}\sum_{j=1}^{i-1}\frac{1}{|\mathbf{r}_i - \mathbf{r}_j|} - \frac{1}{2}\sum_{I=1}^{N_n}\frac{1}{M_I}\nabla_{\mathbf{R}_I}^2 + \sum_{I=1}^{N_n}\sum_{J=1}^{I-1}\frac{Z_I Z_J}{|\mathbf{R}_I - \mathbf{R}_J|}, \tag{2.6}$$

where $\nabla_{\mathbf{r}_i}^2$ and $\nabla_{\mathbf{R}_I}^2$ are the Laplacians with respect to the electronic and nuclear coordinates, $Z_I$ and $M_I$ are the atomic number and mass of the $I^{th}$ nucleus in atomic units, respectively, and the

inner sums run from 1 to $i - 1$ or $I - 1$ to avoid double-counting. Noting that $i, j \in \{1, \dots, n_e\}$ and $I, J \in \{1, \dots, N_n\}$, we may rewrite (2.6) in the form

$$\hat{\mathcal{H}} = -\frac{1}{2} \sum_i \nabla^2_{\mathbf{r}_i} - \sum_i \sum_I \frac{Z_I}{|\mathbf{r}_i - \mathbf{R}_I|} + \frac{1}{2} \sum_{i \neq j} \frac{1}{|\mathbf{r}_i - \mathbf{r}_j|} - \frac{1}{2} \sum_I \frac{1}{M_I} \nabla^2_{\mathbf{R}_I} + \frac{1}{2} \sum_{I \neq J} \frac{Z_I Z_J}{\mathbf{R}_I - \mathbf{R}_J}, \quad (2.7)$$

where the factors of one half in the electron-electron and nuclei-nuclei repulsive potentials account for any double counting in the summations.

## 2.2 Born-Oppenheimer Approximation

In the previous section we saw how we can describe a many-body system in terms of the electronic and nuclear coordinates and spins. In this section we will see how we can approximate (2.3) to a simpler expression in terms of the electronic positions alone. This is accomplished by considering the nuclei-to-electron mass ratio $m_n/m_e \approx 1836.15267389$, so that a nuclei is more than three orders of magnitude heavier than an electron. This means nuclei will be much slower than electrons at the same temperature.[36] In other words, electrons will very rapidly relax to their instantaneous ground-state configuration before the nuclei have had time to move. In this way we can assume that the nuclei are basically stationary and solve for the electronic ground-state first, and then calculate the energy of the system in that configuration and solve for the nuclear motion classically. This is known as the Born-Oppenheimer approximation.[37]

With these assumptions (2.3) takes the form

$$\left[ -\frac{1}{2} \sum_i \nabla^2_{\mathbf{r}_i} - \sum_i \sum_I \frac{Z_I}{|\mathbf{r}_i - \mathbf{R}_I|} + \frac{1}{2} \sum_{i \neq j} \frac{1}{|\mathbf{r}_i - \mathbf{r}_j|} + \frac{1}{2} \sum_{I \neq J} \frac{Z_I Z_J}{|\mathbf{R}_I - \mathbf{R}_J|} \right] \Psi = E_{\text{tot}} \Psi \quad (2.8)$$

Note that in (2.8) the term that describes the kinetic energy of the nuclei, $\hat{T}_n$, in (2.7) has been neglected because the mass of the nuclei are much greater than that of an electron, so that $M_I \gg 1 \; \forall \, I \in \{1, N_n\}$. Assuming this, we can re-scale the total energy of the system and making further modifications we obtain the following equation for the many-body problem in terms of the electronic Hamiltonian $\hat{\mathcal{H}}_e$

$$\hat{\mathcal{H}}(\mathbf{r}_1, \dots, \mathbf{r}_{n_e}) \psi(\mathbf{r}_1, \dots \mathbf{r}_{n_e}) = \varepsilon \psi(\mathbf{r}_1, \dots \mathbf{r}_{n_e}), \quad (2.9)$$

where $\psi$ only depends on the nuclear coordinates parametrically *via* the electron-nuclear potential $V_{e-n}$. Taking this into account we obtain the following equalities

$$\varepsilon = E_{\text{tot}} - \frac{1}{2} \sum_{I \neq J} \frac{Z_I Z_J}{|\mathbf{R}_I - \mathbf{R}_J|}, \tag{2.10}$$

$$V_{e-n}(\mathbf{r}_i) = \sum_I \frac{Z_I}{|\mathbf{r}_i - \mathbf{R}_I|}, \tag{2.11}$$

$$\hat{\mathcal{H}}_0(\mathbf{r}_i) = -\frac{1}{2} \nabla^2_{\mathbf{r}_i} + V_{e-n}(\mathbf{r}_i), \tag{2.12}$$

$$\hat{\mathcal{H}}_e(\mathbf{r}_1, \ldots, \mathbf{r}_{n_e}) = \sum_i \hat{\mathcal{H}}_0(\mathbf{r}_i) + \frac{1}{2} \sum_{i \neq j} \frac{1}{|\mathbf{r}_i - \mathbf{r}_j|}, \tag{2.13}$$

where $\hat{\mathcal{H}}_0$ is the independent electron Hamiltonian.

## 2.3 Periodic Systems

Once we have reduced the Schrödinger equation to a more manageable form, we come to one of the most important properties of materials, namely, periodicity. This property helps us to minimize the number of calculations required to solve (2.9) based on Bloch's theorem.

This theorem states that instead of working in terms of long-ranged spatially dependent wave functions of a system spanning over many atoms, one may consider wave functions with the same periodicity as the primitive unit cell. One advantage of using this unit cell is that by repeating it a sufficient number of times, the initial system is recovered.

Bloch showed that this important theorem gives the following special solution to the Schrödinger equation

$$\psi_{\mathbf{k}}(\mathbf{r}) = u_{\mathbf{k}}(\mathbf{r}) e^{i\mathbf{k} \cdot \mathbf{r}}, \tag{2.14}$$

where $\mathbf{k}$ are samplings within the first Brillouin zone in reciprocal space[38], $u_{\mathbf{k}}(\mathbf{r})$ respects the periodicity of the unit cell so that $u_{\mathbf{k}}(\mathbf{r}) = u_{\mathbf{k}}(\mathbf{r} + \mathbf{T})$, where $\mathbf{T}$ is a translation vector of the lattice. This is a linear combination of the three vectors of the unit cell, so that

$$\mathbf{T} = n_1 \mathbf{a}_1 + n_2 \mathbf{a}_2 + n_3 \mathbf{a}_3, \tag{2.15}$$

where $n_i \in \mathbb{Z}^+$ and the periodicity of a lattice is observed with respect to the primitive lattice vectors $\mathbf{a}_i$.

Both the kinetic energy operator and the Coulomb interaction of the Hamiltonian remain unchanged under a translation $\mathbf{T}$. This means the Hamiltonian of a periodic system commutes with translations, so that they have the same eigenstates. Moreover, this results in eigenstates that can be labeled according to their translational symmetry.

A consequence of Bloch's theorem is that all observables of the systems can be Fourier expanded in terms of the reciprocal lattice vectors $\mathbf{G}$.

$$\mathbf{G} = m_1 \mathbf{b}_1 + m_2 \mathbf{b}_2 + m_3 \mathbf{b}_3 \tag{2.16}$$

where $m_i \in \mathbb{Z}^+$ and $\mathbf{b}_i$ are the reciprocal vectors of the lattice

$$\mathbf{b}_i = 2\pi \frac{\mathbf{a}_j \times \mathbf{a}_k}{\Omega}, \tag{2.17}$$

where $\Omega$ is the volume of the unit cell. The relation between the vectors of the unit and the reciprocal lattice cell is then

$$\mathbf{a}_i \cdot \mathbf{b}_j = 2\pi \delta_{ij}, \tag{2.18}$$

so that

$$\exp\left(i\mathbf{G_m} \cdot (\mathbf{r} + \mathbf{R_n})\right) = \exp\left(i\mathbf{G_m} \cdot \mathbf{r}\right). \tag{2.19}$$

The Fourier expansions of $V_{ext}$ and other periodic functions, e.g., $u_{n,\mathbf{k}}(\mathbf{r})$, are then,

$$u_{n,\mathbf{k}}(\mathbf{r}) = \sum_{\mathbf{G_m}} e^{i\mathbf{G_m} \cdot \mathbf{r}} u_{n,\mathbf{k}}(\mathbf{G_m}). \tag{2.20}$$

In order to ensure the normalization of Bloch waves in (2.14), we must restrict the values of $\mathbf{k}$ and the number of particles. To do this, boundary conditions must be satisfied, i.e.,

$$\psi_{n,\mathbf{k}}(\mathbf{r} + N_i \mathbf{a}_i) = \psi_{n,\mathbf{k}}(\mathbf{r}), \tag{2.21}$$

yielding a restriction for $\mathbf{k_l}$ of

$$\mathbf{k_l} = \frac{l_1}{N_1}\mathbf{b}_1 + \frac{l_2}{N_2}\mathbf{b}_2 + \frac{l_3}{N_3}\mathbf{b}_3 \quad \text{and} \quad -\frac{N_i}{2} \leq l_i < \frac{N_i}{2}, \tag{2.22}$$

where $l_i \in \mathbb{Z}^+$. These constrained values of $\mathbf{k}$ correspond to the first Brillouin zone. Calculations to represents Kohn-Sham (KS) wavefunctions by using Bloch waves a finite number of points are required within the first Brillouin zone. A Monkhorst-Pack sampling[39] of special[40] $k$-points is performed as it is an unbiased method to select these points in an equally spaced mesh

$$\mathbf{k}(n_1, n_2, n_3) = \sum_{i=1}^{3} \frac{2n_i - N_i - 1}{2N_i} \mathbf{b}_1, \tag{2.23}$$

where $n_i \in \{1, \ldots, N_i\}$, and $N_i$ denotes the number of points sampled in the $\mathbf{b}_i$ direction.

The calculation of many properties requires the evaluation of integrals over the Brillouin zone in reciprocal space. This discrete set of $\mathbf{k}$-points allows us to accurately approximate of these integrals[41]. To illustrate this, the integral of a function $F(\mathbf{k})$

$$\frac{1}{\Omega_{\mathrm{BZ}}} \int_{\mathrm{BZ}} F(\mathbf{k}) d\mathbf{k} \approx \sum_{\mathbf{k}} w_{\mathbf{k}} F(\mathbf{k}), \tag{2.24}$$

is approximately equal to the weighted sum over the k-points of the first Brillouin zone, where $\Omega_{\mathrm{BZ}}$ is the volume of the Brillouin zone and $w_{\mathbf{k}}$ is the weight of $k$-point $\mathbf{k}$. It is also important to note that symmetries within the unit cell, including the necessary time-reversal symmetry, may be imposed to reduce the Brillouin zone to the irreducible Brillouin zone (IBZ), wherein all $k$-points of the first Brillouin zone map be mapped. This is accounted for by adjusting the weights $w_{\mathbf{k}}$ of each $k$-point within the IBZ.

## 2.4  Hohenberg-Kohn Theorem

One of the most widely used ways to reduce the computational effort of calculating the many-body wave function of the positions of all electrons is to work in terms of the electronic density. The Hohenberg-Kohn theorem tells us why such a different approach may be used.

The Hamiltonian in (2.8) is completely determine by the $n_e$ electrons and the external potential $V_{ext}$, as is the ground state electronic wavefunction $\psi_0$. Similarly, the ground state electronic density $n_0(\mathbf{r})$ is a functional of the number of electrons $n_e$ and the external potential $V_{ext}$, so that

$$n_0(\mathbf{r}) = \langle \psi_0 | \hat{n} | \psi_0 \rangle = \int \cdots \int \left| \psi_0(\mathbf{r}, \mathbf{r}_2, \ldots, \mathbf{r}_{n_e}) \right|^2 d\mathbf{r}_2 \ldots d\mathbf{r}_{n_e}, \tag{2.25}$$

where $\hat{n}$ is the density operator. From these observations we may obtain the Hohenberg-Kohn theorem, which is the foundation of density functional theory (DFT)[42].

**Theorem 1** (Hohenberg-Kohn). The ground state electronic density $n_0(\mathbf{r})$ is uniquely determined by the corresponding external potential $V_{ext}(\mathbf{r})$, to within an additive constant.

The proof of the Hohenberg-Kohn theorem is rather straightforward and may be found in Ref. 36. Moreover, the ground state is a unique functional of the ground state density

$$|\psi_0\rangle = |\psi\,[n_0]\rangle. \tag{2.26}$$

However, such a functional dependence can be extremely complicated. The existence of this functional means that any ground state observable $\hat{O}$ is also a functional of the density, so that

$$\hat{O}[n] \equiv \langle\psi[n]|\hat{O}|\psi[n]\rangle. \tag{2.27}$$

In particular, this holds for the ground state energy $E_{gs}$, which will be the most important density functional,

$$E_{gs}[n] \equiv \langle\psi[n]|\hat{\mathcal{H}}|\psi[n]\rangle = \mathcal{F}[n] + \int d^3\mathbf{r}\,V_{ext}(\mathbf{r})n(\mathbf{r}), \tag{2.28}$$

where $\mathcal{F}[n]$ corresponds to a universal functional for all systems

$$\mathcal{F}[n] \equiv \left\langle\psi[n]\left|\left(\hat{T}_e + V_{e-e}\right)\right|\psi[n]\right\rangle, \tag{2.29}$$

and $V_{ext}$ enters into $E_{gs}[n]$ at only one point.

Another fundamental concept within DFT is the minimum principle for the ground state energy functional $E_{gs}[n]$. For all densities $n_0'(\mathbf{r}) \neq n_0(\mathbf{r})$, where $n_0$ is the ground state density corresponding to $V_{ext}$,

$$E_{gs}\,[n_0] < E_{gs}\,[n_0'] \quad\Leftrightarrow\quad E_0 = \min_{n\in\mathcal{N}} E_{gs}[n], \tag{2.30}$$

where $\mathcal{N}$ is the set of all ground state densities corresponding to different external potentials $V_{ext}$. This principle is a direct consequence of the Ritz variational principle, that is, the ground state

$\left|\psi_0'\right\rangle$ corresponding to $n_0'$ is not the same as $|\psi_0\rangle$. The functional $E_{gs}[n]$ has its domain restricted to only densities in $\mathcal{N}$, as obtained by solving (2.8)[43].

The ground state energy functional can be rewritten as

$$E_{gs}[n] = T[n] + E_{\mathrm{H}}[n] + E_{ext}[n] + E_{xc}[n], \tag{2.31}$$

that is, as the sum of the kinetic energy functional $T[n]$, the Hartree interaction energy functional $E_{\mathrm{H}}[n]$, the external potential energy functional $E_{\mathrm{ext}}[n]$ and the exchange and correlation (xc) energy functional $E_{xc}[n]$. The xc functional accounts for the complicated effects of the interactions not present in $T$, $E_{\mathrm{H}}$, or $E_{ext}$.

## 2.5   Kohn-Sham Self-Consistent Field Approach

The basic idea behind the Kohn-Sham (KS) approach[44], which makes DFT computationally feasible, is to introduce a complete mapping of the interacting many-body problem onto a suitable non-interacting system, i.e., the KS system[44]. This fictitious system of non-interacting electrons is assumed to have a ground state density that is the same as the density of the fully interacting system. The ground state density $n_0(\mathbf{r})$, energy $E_{gs}$, and forces $\mathbf{F}_I$ between the nuclei can be obtained through the KS self-consistent field procedure. The KS scheme consists of the following five steps:

1. An initial guess $n_0$ for the trial density $\tilde{n}(\mathbf{r})$ is made.

2. The effective potential

$$V_{\mathit{eff}}[\tilde{n}](\mathbf{r}) = V_{ext}(\mathbf{r}) + \int \frac{\tilde{n}(\mathbf{r}')}{|\mathbf{r} - \mathbf{r}'|} d^3\mathbf{r}' + V_{xc}[\tilde{n}](\mathbf{r}), \tag{2.32}$$

   is calculated, where $V_{ext}(\mathbf{r})$ is the external potential due to the nuclei, the second term corresponds to the Hartree potential from the other electrons, and the third term $V_{xc}$ is the exchange and correlation (xc) potential. The Hartree[45] potential's source is the average density of the electrons, and the xc term includes corrections to the kinetic energies and electron-electron interactions. Effectively, $V_{xc}$ is the difference between Hamiltonians that describe fully interacting electrons and the independent electrons of the KS system.

3. The independent-electron Schrödinger equation is solved to obtain the KS wavefunctions $\varphi_i$, where the effective potential $V_{ext}[\tilde{n}]$ is previously obtained functional of the trial density, so that

$$\left(-\frac{1}{2}\nabla^2 + V_{eff}[\tilde{n}](\mathbf{r}) - \epsilon_i\right)\varphi_i(\mathbf{r}) = 0. \tag{2.33}$$

4. A new trial density $\tilde{n}'(\mathbf{r})$ is calculated from the KS wavefunctions $\varphi_i$ obtained from the last step. To obtain the density only the $n_e/2$ lowest eigenfunctions $\varphi_i$ need to be summed if the system is spin-paired

$$\tilde{n}'(\mathbf{r}) = 2\sum_{i=1}^{n_e/2} |\varphi_i|^2 . \tag{2.34}$$

5. Steps (2), (3), and (4) are repeated until the density is converged, that is, the trial density $\tilde{n}'(\mathbf{r})$ is approximately equal to $\tilde{n}(\mathbf{r})$, the previous density from Eq. (2.34), up to a defined accuracy. Once this is achieved, we have a "final" density $n(\mathbf{r})$ with the corresponding eigenenergies $\epsilon_i$.

This cycle is also shown schematically in Fig. 2.1.

The occupied KS wavefunctions $\varphi_i$ yield the ground state density of our system and $\epsilon_{n_e/2}$ the eigenvalue corresponding to the highest occupied molecular orbital (HOMO), is the system's ionization energy. The ground state energy $E_{gs}$ can be calculated from the outputs of the KS scheme using

$$E_{gs} = \sum_{i=1}^{N/2} \epsilon_i + E_{xc}[n] - \int v_{ext}(\mathbf{r})n(\mathbf{r})d^3\mathbf{r} + \frac{1}{2}\iint \frac{n(\mathbf{r})n(\mathbf{r}')}{|\mathbf{r} - \mathbf{r}'|}d^3\mathbf{r}d^3\mathbf{r}'. \tag{2.35}$$

It is important to mention that, so far, the xc potential $V_{xc}$ only has an exact expression for systems with a few atoms. This means that, in the case of a many-body problem, the xc functional must be approximated.

Finally, in order to find the relaxed structure of a system, it is necessary to minimize the forces on its atoms. The force acting on an atom at $\mathbf{R}_I$ is $\mathbf{F}_I = -\nabla_{\mathbf{R}_I}E_{gs}[n]$.[43] By the Hellman-Feynman theorem[46], we can also calculate the ionic forces using $\mathbf{F}_I = -\left\langle\psi_0\left|\nabla_{\mathbf{R}_I}\hat{\mathcal{H}}\right|\psi_0\right\rangle$. This means we can obtain the forces from the ground state KS wavefunctions which were already calculated
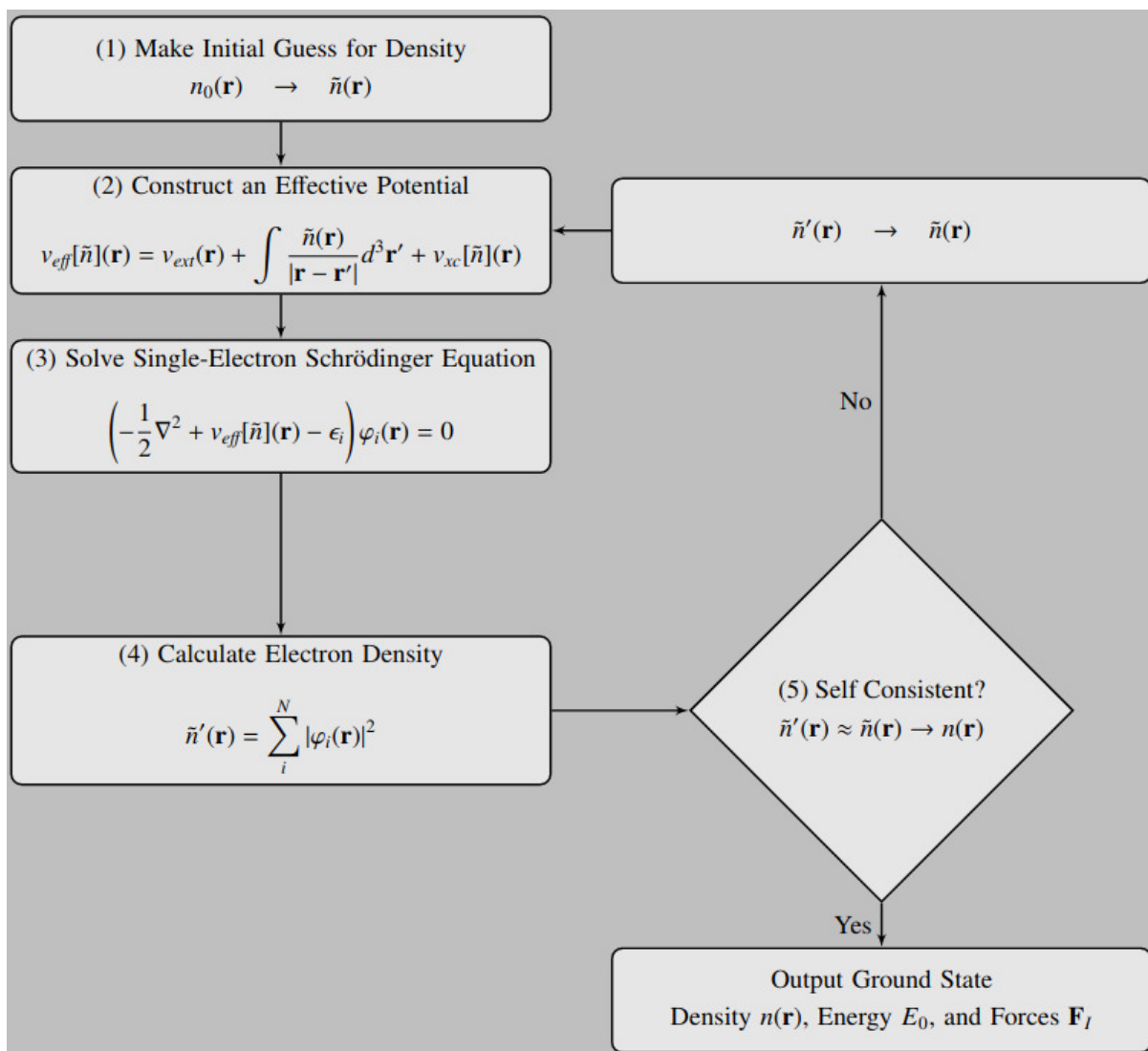
Figure 2.1: Kohn-Sham system to obtain the ground state density $n(\mathbf{r})$, energy $E_0$ and forces $\mathbf{F}_i$

within the KS self-consistent scheme. It is important for us to recall that here the total energy depends parametrically on the positions of the nuclei.

## 2.6 Exchange Correlation Functionals

According to the KS scheme, an effective potential must be constructed to then solve the Schrödinger equation for an independent electron. The effective potential consists of an external potential, the Hartree potential and the local xc potential, as shown in (2.36)

$$V_{eff}[\tilde{n}](\mathbf{r}) = V_{ext}(\mathbf{r}) + \int \frac{\tilde{n}(\mathbf{r}')}{|\mathbf{r} - \mathbf{r}'|} d^3\mathbf{r}' + V_{xc}[\tilde{n}](\mathbf{r}). \tag{2.36}$$

The xc energy $E_{xc}$ corresponding to a particle at position $\mathbf{r}$ can be assumed to mainly depend on the electron density $n(\mathbf{r}')$ at position $\mathbf{r}'$ near $\mathbf{r}$. In other words, the xc energy can be assumed to be a local function. More quantitatively, the xc energy depends on the density within a neighbourhood with a radius of the Fermi wavelength $\lambda_F$, where

$$\lambda_F(\mathbf{r}) = \frac{2\pi}{\sqrt[3]{3\pi^2 n(\mathbf{r})}}, \tag{2.37}$$

the shortest de Broglie wavelength for non-interacting electrons. This suggests the xc energy is a localized functional of $n(\mathbf{r}')$ and has a quasi-local description.

### 2.6.1 Local density approximation

If we assume the exchange energy is completely local, i.e., it depends only on the density at the same location ($\mathbf{r}' = \mathbf{r}$), we obtain the local density approximation (LDA). In this case the xc energy satisfies

$$E_{xc}^{LDA} = \int \epsilon_{xc}^{LDA}[n] n(\mathbf{r}') d^3\mathbf{r}' \tag{2.38}$$

where $\epsilon_{xc}^{LDA}[n]$ is the xc energy of a uniform electron gas with density $n$. This is because the xc energy of a uniform electron gas has no spatial dependence by definition. LDA is obviously exact for a uniform electron gas, by construction. However, for atomic systems, where the densities are not slowly varying and electron-electron interactions become important, such as in heavy fermion systems, LDA often fails. Nevertheless, LDA gives useful results for most applications with surprising accuracies of 1% for the bond-lengths and geometries of molecules and solids.

As discussed in Ref. 47, LDA is widely used to realize the Kohn-Sham scheme since the exchange correlation potential is a simple function of the local density,

$$V_{xc}^{LDA}(\mathbf{r}) = \frac{\delta E_{xc}^{LDA}[n]}{\delta n}, \tag{2.39}$$

where $\frac{\delta}{\delta n}$ denotes the functional derivative with respect to the density $n$.

Physically, $V_{xc}^{LDA}$ can act in an extremely short range because it depends on the local density. The LDA discards the corrections to the energy xc since there are inhomogeneities, but it is very useful despite this approximation. The use of LDA in DFT has been for a number of years in which a great number of successful results have been produced. Furthermore, the errors caused by the overestimation of the correlation energy and the underestimation of the exchange energy by the LDA, commonly cancel each other. One of the most notable disadvantages of LDA is the excessive binding of molecules.[48]

## 2.6.2 Generalized gradient approximation

In order to take into account non-homogeneities in the electron density, a semi-local approximation that depends on the gradient of the density is often used. These types of generalized gradient approximations (GGA) are based on how the density changes away from the coordinate. The GGA exchange functional generally takes the form[49]

$$E_x^{GGA}[n] = \int \epsilon_x^{HEG}\left(n_0 = n(\mathbf{r})\right) F_x[s(\mathbf{r})] d^3\mathbf{r}, \tag{2.40}$$

where $n(\mathbf{r})$ is the electronic density, $\epsilon_x^{HEG}$ is the exchange energy density of a homogeneous electron gas (HEG), i.e., $\sim n^{4/3}$, $F_x$ is an enhancement factor, and $s$ is the dimensionless density gradient

$$s = \frac{|\nabla n|}{2k_F n}, \tag{2.41}$$

where $k_F = \sqrt[3]{3\pi^2 n}$. It is important to note that although (2.39) is spin-unpolarized, a spin-polarized version may also be deduced[49].

The enhancement for any GGA that recovers the HEG limit is

$$F_x[s] \approx 1 + \mu s^2 + \cdots \tag{2.42}$$

as $s \rightarrow 0$.

Similarly, the gradient expansion for the correlation functional that recovers the HEG limit is

$$E_c^{\text{GGA}}[n] = \int n(\mathbf{r}) \left\{ \epsilon_c^{\text{HEG}}[n(\mathbf{r})] + \frac{\pi k_F}{2} \beta s^2 [n(\mathbf{r})] + \cdots \right\} d^3\mathbf{r}, \tag{2.43}$$

where $\epsilon_c^{\text{HEG}}$ is the correlation energy of the HEG and $\beta$ is a coefficient.

GGA functionals have often been parametrized by fitting experimental data, but were then restricted in their application to certain systems. However, parameter-free functionals can be used in a wide range of systems. Some of the most commonly used examples of such *ab initio* functionals are those developed by Perdew, Burke, and Ernzerhof (PBE)[49,50].

## PBE GGA

The parameters used in the PBE GGA functional[49] are rather fundamental constants and are defined as

$$\mu = 0.21951 \text{ and } \beta = 0.0066725. \tag{2.44}$$

The PBE functional used includes the linear response of the uniform gas, the correct behavior under uniform scaling, and a smoother potential. More details about the PBE functional and the consequences in practical calculations are found in Refs. 51 and 52.

## PBEsol GGA

The PBEsol functional is a revised PBE GGA that improves the equilibrium properties of densely packed solids and their surfaces[50]. For this xc functional, the same form as PBE is used but the parameters are set to

$$\mu = \mu_{GE} = 0.1235 \text{ and } \beta = 0.046, \tag{2.45}$$

where $\mu_{GE}$ is used to obtain an accurate gradient expansion for slowly varying electrons. PBEsol reduces the dependence on error cancellation by providing a more accurate description for both

exchange and correlation energies of surfaces. The performance of PBEsol for solids is assessed in Ref. 50.

**PBE-D3**

Although the PBE xc functional provides a good approximation to the binding energies of chemisorbed systems, it often does not provide a good description of physisorption processes as it does not consider van der Waals (vdW) interactions. To address this issue, the energy correction term proposed by Grimme *et al.*[53] may be used

$$E_{\text{disp}} = -\frac{1}{2} \sum_{i=1}^{N_n} \sum_{j=1}^{N_n} \sum_{L} \left( f_{d,6} \left( r_{ij,L} \right) \frac{C_{6ij}}{r_{ij,L}^6} + f_{d,8} \left( r_{ij,L} \right) \frac{C_{8ij}}{r_{ij,L}^8} \right), \qquad (2.46)$$

where the dispersion coefficients $C_{6ij}$ are dependent on the atomic species and geometry as they are adjusted on the basis of the local geometry (coordination number) around atoms $i$ and $j$. In the zero-damping variant of the DFT-D3 method (DFT-D3(zero)), the damping function reads:

$$f_{d,n} \left( r_{ij} \right) = \frac{s_n}{1 + 6 \left( r_{ij} / \left( s_{R,n} R_{0ij} \right) \right)^{-\alpha_n}} \qquad (2.47)$$

where $R_{0ij} = \sqrt{C_{8ij}/C_{6ij}}$, the parameters $\alpha_6 = 14$, $\alpha_8 = 16$, $s_{R,8} = 11$, and $s_6 = 1$ are fixed while $s_8$ and $s_{R,6}$ are parameters whose values depend on the choice of xc functional.

## 2.7   Representation of the Khon-Sham wavefunctions

In DFT calculations, generally one of three types of representations of the KS wavefunctions are used: real space (RS), plane waves (PWs), and linear combinations of atomic orbitals (LCAOs). For RS representations the wavefunctions are directly sampled at a finite number of grid points, whereas for PW or LCAO representations, the wavefunctions are expanded in either a plane wave or atomic orbital basis set, respectively.

A wavefunction is an element of a Hilbert space, that is, a vector space with an inner product. States are represented as elements of this vector space and therefore can be expressed as a linear

combination of basis vectors. Moreover, any state $\psi$ can be expressed as the linear combination of vectors of a complete basis set $\{\phi_\mu\}$

$$\psi_n = \sum_\mu c_{n,\mu}\phi_\mu. \tag{2.48}$$

In practice, a truncated basis set is used to expand the wavefunctions and find the solution to the KS equation in such a way that a finite matrix is employed to solve the eigenvalue problem. In this section we provide a very brief review of each of these three representations.

### 2.7.1 Real Space

The values of wavefunctions, electron densities, and potentials on a discrete grid of finite points in real space can be used to represent them[54,55]. Also, the kinetic operator of the Hamiltonian contains the Laplacian operator and involves derivatives that may be approximated by finite difference (FD) techniques[56]. The accuracy of this method can be systematically improved by increasing the number and density of grid points, i.e., decreasing the spacing of the grid. One of the advantages of this method is its flexibility when imposing boundary conditions. They can be either periodic, non-periodic, or a mixture of the two. Furthermore, RS calculations can be parallelized on different processors by domain decomposition. In this way the RS or FD representation of the KS wavefunctions can be easily scaled up to perform calculations that involve very large molecules with a great number of atoms.

### 2.7.2 Plane Waves

As we have seen in section 2.3, plane waves can constitute a complete basis set that spans the space of KS wavefunctions. For a given unit cell of volume $\Omega$ and $k$-point $\mathbf{k}$ we may express the periodic part of the wavefunction $u_n$ from (2.14) using (2.20) as

$$u_n(\mathbf{r}) = \frac{1}{\sqrt{\Omega}} \sum_{\mathbf{G}} \tilde{u}_{n,\mathbf{G}} e^{i\mathbf{G}\cdot\mathbf{r}}. \tag{2.49}$$

In this way, the KS wavefunctions can be represented in terms of the coefficients $\tilde{u}_{n,\mathbf{G}}$, and the quality of this description is systematically improved by inclusion of more reciprocal lattice

vectors, $\mathbf{G}$, in the sum of (2.49). However, a PW expansion of the KS wavefunctions cannot be domain decomposed, as is possible for real space calculations. This means paralelization may only be performed over bands and $k$-points. Overall, PW representations are best suited for the description of periodic systems, such as solids, and have difficulties describing localized isolated systems. Despite this, the implied restriction of (2.49) on the form which the wave functions may take tends to yield an improved and more dependable convergence of the KS scheme compared to RS representations.

### 2.7.3   Linear Combination of Atomic Orbitals

Another type of basis set that can be used to represent the KS wavefunctions are linear combinations of atomic orbitals (LCAOs). This approximation is widely used for *ab initio* calculations, and is based on the idea that the molecular orbitals of a given system can be built from the orbitals of its constituent atoms[57]. The representation of the KS wavefunctions as a linear combination of atom-centered functions has proven to be useful in large systems with many atoms per unit cell or with vacuum regions where plane waves become computationally expensive to use[58]. For instance, the GPAW code employs LCAOs as a basis within the projector-augmented wave (PAW) method[59].

An atomic orbital centered on atom $a$, located at $\mathbf{r}_a$, $\phi^a_{nlm}(\mathbf{r} - \mathbf{r}_a)$, is the product of a numerical radial function $\zeta_{nl}(r)$ and a spherical harmonic $Y_{lm}(\theta, \varphi)$, so that

$$\phi^a_{nlm} = \zeta_{nl}(r)Y_{lm}(\theta, \varphi), \tag{2.50}$$

where $\{r, \theta, \varphi\}$ are spherical coordinates centered on atom $a$. In this way, $\mu$ in (2.48) corresponds to atom $a$ and $n$, $l$, and $m$, the three quantum numbers of a state. This basis set is obtained by solving the radial all-electron KS equations for isolated atoms[60,61]. The detailed procedure to generate LCAO basis functions can be found in Ref. 62.

LCAO basis sets are named following the number of basis functions used for each element[59,63]. In this way, for the minimal or single-$\zeta$ (SZ) basis set, one radial function $\zeta_{nl}(r)$ for each occupied valence orbital, $|n\rangle$, is included. Likewise, multiple-$\zeta$ sets are obtained by generating multiple functions by the split valence technique for each occupied valence orbital[64]. For instance, the SZ

basis set for a hydrogen atom has one *s*-type function and the DZ basis set for a carbon atom has two *s*-type functions and $2 \times 2p$-type functions.

Multiple-$\zeta$ orbitals improve the radial flexibility of the basis set and polarization functions that have higher angular momentum *l* improve the angular flexibility. A polarized basis set has a function with angular momentum $l + 1$ where *l* is the highest occupied valence orbital. For example, a DZP basis for carbon or  has 8 functions from the DZ part and 5 functions from the polarized part which is a *d*-type orbital[63], yielding a total of 13 orbitals per atom.

## 2.8   Projector Augmented Wave Method

The KS equations can be solved using efficient numerical methods by means of approximations, which are related to the behavior of the wave functions in the different possibilities of space, that is, near and far from the nucleus. These are known as pseudopotential methods and all-electron method.

The implementation of pseudopotentials and pseudowave functions is based on the observation that the electrons closest to the nucleus have a low interaction with the chemical environment. This tells us that the energy possessed by the electrons closest to the nucleus is approximately the same whether the atoms are isolated or forming a molecule. Furthermore, the total binding energy depends mostly on the energy of the valence electrons and generally does not involve the innermost electrons of the atom. On the other hand, the computational capacity necessary to represent the innermost electrons of atoms is not very efficient to deal with the Coulomb potentials to which they are subjected[65].

All atomic wavefunctions, whether core or valence, should be mutually orthogonal because they are derived from the same atomic Hamiltonian. The valence wavefunctions must oscillate rapidly in the neighborhood of the nucleus to maintain their orthogonality since the states of the nucleus are located in this region. Considering that the kinetic energy is proportional to the second derivatives of the wave function and, therefore, to the magnitude of the curvature, these rapid oscillations result in a high kinetic energy of the valence electrons close to the nucleus. This kinetic energy produced causes the potential energy corresponding to the Coulomb potential

to be annulled and it is for this reason that the valence electrons have greater freedom than the electrons in the nucleus.

For this reason, it is often convenient to replace the Coulomb potential and core electrons with a smooth[66] pseudopotential and reproduce the effect of the potential and core electrons on the valence electrons. To solve the KS equations, only the valence electrons are considered for pseudopotentials, which are calculated and tabulated once for each element. However, this approach has drawbacks since the information of the wave functions near the nucleus is lost and there is no rigorous procedure to obtain reliable pseudopotentials.

In contrast, for all-electron methods the wave function retains all the information. This is because if we use the frozen nucleus approximation, which fixes the orbitals within the nucleus and they are calculated and tabulated once for each isolated atomic species.

The Augmented-Plane-Wave (APW) is a all-electron method which divides space into two regions: a spherical one that is centered on each atom where the wave function expands locally, and an interstitial between atoms where basis sets are usually used as plane waves, so that both basis join at the limits of both regions.[67]

APW is a special case of a general all-electron method called Projector Augmented Wave (PAW).[68]. This method is implemented within the GPAW[69] code in all the calculations presented in this thesis. The PAW method establishes a linear transformation $\hat{\mathcal{T}}$ that maps the physical valence wavefunctions $\psi_n$ onto computationally convenient fictitious pseudowavefunctions $\tilde{\psi}_n$,

$$\psi_n = \hat{\mathcal{T}}\tilde{\psi}_n, \tag{2.51}$$

where $n$ is a quantum state label, that is a band, spin, or $k$-vector index. The transformation operator is given by

$$\hat{\mathcal{T}} = 1 + \sum_a \sum_i \left( \left| \phi_i^a \right\rangle - \left| \tilde{\phi}_i^a \right\rangle \right) \left\langle \tilde{p}_i^a \right|, \tag{2.52}$$

where $\phi_i^a$ are the atom-centered partial waves used to expand the all-electron wavefunction within the atom-centered sphere or augmentation region, so that $|\psi_n\rangle = \sum_{ai} c_{ni}^a |\phi_i^a\rangle$, $\tilde{\phi}_i^a$ are the corresponding partial waves used to expand the pseudowavefunctions, and $\tilde{p}_i^a$ are projector functions.

The approximation of the pseudo partial wave with the true partial wave is sufficiently precise outside the augmentation region and smooth continuations within it. For each pseudo partial

wave, a projector function is established which is located within the magnification region and satisfies the condition $\left\langle \tilde{p}_i^a \mid \tilde{\phi}_j^a \right\rangle = \delta_{ij}$ inside the sphere. For the PAW method to prove to be practical, approximations such as the frozen core need to be considered.

## 2.9 Non-equilibrium Green's function methods

To understand the dynamics of chemical bonds between molecules, methods have been developed that facilitate calculations of electronic transport (ET) and that are responsible for the chemical process behind any reaction. The first experiments performed were in the ET 2000s, where transport across molecular cable junctions was measured[70,71]. The general scientific interest to understand the dynamics between bonds, led to the development of theoretical methods that have a high reliability to simulate ET through nanoscale bonds.

DFT provides a convenient framework for performing *ab initio* calculations for a wide range of systems. However, most of these methods used in calculations must be limited to finite or periodic systems in equilibrium. Furthermore, a rigorous theory capable of using a more appropriate[72] functional has not yet been developed.

For physical systems to show ET, a bias with finite voltage must must be applied to the electrons in the junction, which is transported across the junction. This results in highly elastic dispersion through a system that is not in equilibrium.

The basis of the ET calculation methods is based on the Landauer[73,74] and Büttiker[75] formulation used to explain the current through a finite disordered region of non-interacting electrons. The conductance formulated by Landauer-Büttiker can be solved using the non-equilibrium Green's function (NEGF) method where the ground state of the system Hamiltonian is gets from DFT. In this section, we will describe this method.

### 2.9.1 Electronic transport in a contact-electrode system

If we consider the low temperature limits ($T \rightarrow 0$) and zero bias ($\epsilon \approx \varepsilon_F$), the linear response conductance of non-interacting electrons passing through a scattering region ($C$) connected by

two input and output electrodes (*input*, *output*) we can define it as

$$G = G_0 T\left(\varepsilon_F\right), \tag{2.53}$$

where $T(\epsilon)$ is the elastic transport function, $\varepsilon_F$ is the Fermi energy, and $G_0 = 2e^2/h = 2/\pi$ is the quantum of conductance. The probability that electrons with a given energy $\epsilon_i$ can be transferred across a junction is described by the elastic transport function. The retarded, $\mathcal{G}^r$, and advanced, $\mathcal{G}^a$, Green's functions (GFs) are defined in terms of a spatially localized basis set $\{\phi_i\}$ chosen to represent the system's Hamiltonian $\hat{\mathcal{H}}$ and the current, and may be expressed in term of the input and output leads and the scattering region as

$$(z^r \mathcal{S} - \mathcal{H})\mathcal{G}^r = 1, \tag{2.54}$$

where $z^r = \epsilon + i0^+$ is the pole of the retarded GF $\mathcal{G}^r$, $\mathcal{H}$ is the Hamiltonian matrix, $\mathcal{S}$ is the coupling matrix and 1 is the identity matrix. The advanced GF can be obtain by applying the complex conjugate transform to the retarded GF, so that $\mathcal{G}^a = (G^r)^\dagger$. Equation (2.54) describes the system as one of non-interacting electrons moving phase-coherently through a scattering region from a input to output lead. Meir and Wingreen[76] derived a useful formula for the transmission function using NEGF in term of the regions $input - C - output$,

$$T(\epsilon) = \mathrm{Tr}\left[\mathcal{G}_C^r(\epsilon)\Sigma_{\mathrm{input}}(\epsilon)\mathcal{G}_C^a(\epsilon)\Sigma_{\mathrm{output}}(\epsilon)\right] \tag{2.55}$$

where $\mathcal{G}_C^r(\epsilon)\left(G_C^a(\epsilon)\right)$ is the retarded (advanced) GF of the scattering ($C$) region,

$$\mathcal{G}_C^r(\epsilon) = \left[z^r \mathcal{S}_C - \mathcal{H}_C - \Sigma_{\mathrm{input}}\left(z^r\right) - \Sigma_{\mathrm{output}}\left(z^r\right)\right]^{-1}. \tag{2.56}$$

The lead self-energies $\Sigma_{i/o}$ for the *input* or *output* leads in (2.55) are defined as,

$$\Sigma_{i/o}(z) = (z\mathcal{S}_{C,i/o} - \mathcal{V}_{C,i/o})\mathcal{G}_{i/o}^0\left(z\mathcal{S}_{C,i/o}^\dagger - \mathcal{V}_{C,i/o}^\dagger\right) \tag{2.57}$$

where $\mathcal{V}_{C,i/o}$ and $\mathcal{S}_{C,i/o}$ are the coupling and overlap matrices between the scattering region atoms and the $i/o$ lead, respectively, $G_{i/o}^0 = [z\mathcal{S}_{i/o} - \mathcal{H}_{i/o}]^{-1}$ is the surface GF that describes the semi-infinite $i/o$ lead in terms of the Hamiltonian and overlap of the same lead, which can be calculated using a decimation technique[77]. The self energy is calculated similarly using a Dyson equation[78],

where the infinite sum of Feynman diagrams are connected by the GF of the scattering between *input* and *output* leads across the scattering (*C*) region. Finally,

$$\Gamma_{i/o} = i\left(\Sigma_{i/o} - \Sigma_{i/o}^\dagger\right) \tag{2.58}$$

are the off-diagonal eigenenergies for each lead region[79].

## 2.9.2 Algorithmic implementation

An appropriate method for performing ET calculations was implemented by Brandbyge *et al.*[80], as shown schematically in Fig.2.2. Considering *input* − *C* − *output* regions, the density, overlaps, and Hamiltonian matrix of each region are expressed as a full Hamiltonian of the form

$$\mathcal{H} = \begin{pmatrix} \ddots & \mathcal{V}_i & 0 & 0 & 0 \\ \mathcal{V}_i^\dagger & \mathcal{H}_i & \mathcal{V}_i & 0 & 0 \\ 0 & \mathcal{V}_i^\dagger & \mathcal{H}_C & \mathcal{V}_o & 0 \\ 0 & 0 & \mathcal{V}_o^\dagger & \mathcal{H}_o & \mathcal{V}_o \\ 0 & 0 & 0 & \mathcal{V}_o^\dagger & \ddots \end{pmatrix} \tag{2.59}$$

where $\mathcal{H}_i$, $\mathcal{H}_o$, and $\mathcal{H}_C$ are the onsite Hamiltonian matrices of the *input*, *output*, and *C* regions, respectively, and $\mathcal{V}_i$ and $\mathcal{V}_o$ are the coupling matrices between the $i/o$ lead and the *C* region, respectively. This is the formalism employed to describe intratube transport through a single SWCNT (*cf.* Figure 2.2).

Note that the interaction between input and output leads in the scattering region is assumed to be zero. This is because there should be no interaction between non-neighboring principal layers (PLs) of the leads. Also, the leads are continued semi-infinitly along the transmission directions.

The GPAW code implement the strategy of invert the total Hamiltonian in (2.59) as a semi-infinite matrix to obtain the GF[81,82] with the following considerations. As shown in Fig. 2.2, leads typically include at least two PLs in order to separately determine the onsite hamiltonian $\mathcal{H}$ and the coupling between PLs $\mathcal{V}$. This would mean the matrices ($\mathcal{H}_{i/o}$) contain at least two PLs, with one being a periodic part of the Hamiltonian such that there is only coupling between nearest-neighbor PLs. To ensure we have proper interactions between the central (*C*) scattering
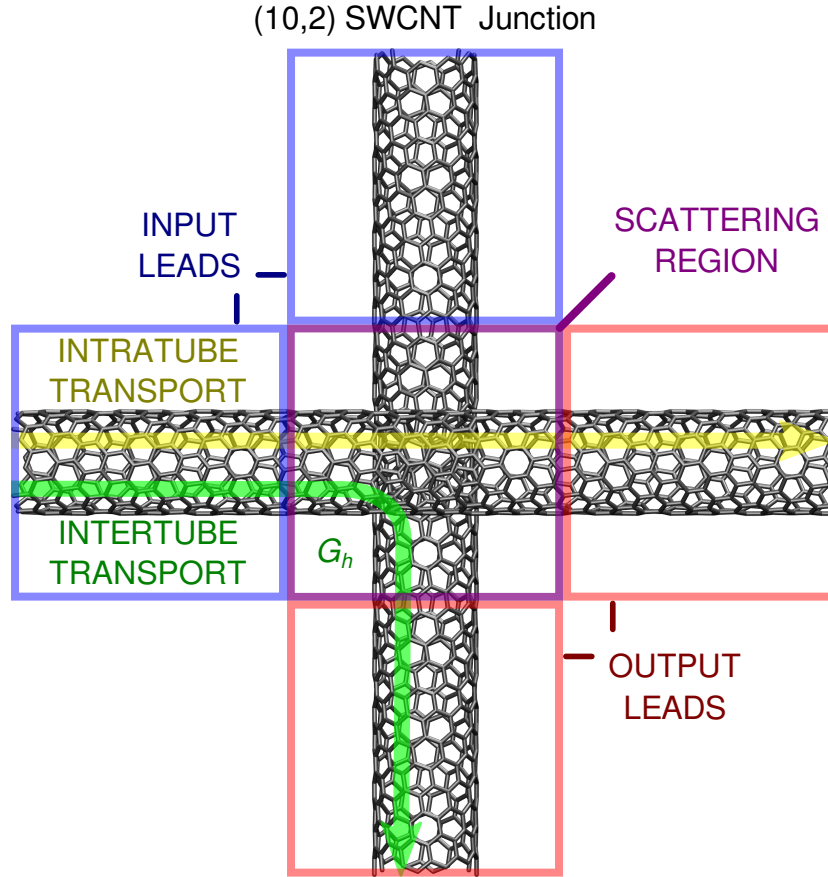
Figure 2.2: Schematic representation of the scattering region in a (10,2) SWCNTs unit cell junction composed of two pairs of input/output electrodes leads, left and right, top and bottom, and a central (C) scattering region, with Hamiltonians $h_1, h_2$ for input/output electrodes pairs, and $h$, for central region. The intratube transport (yellow arrow) and intertube transport (green arrow) processes are depicted schematically with hopping conductance $G_h$

region and the electrodes or leads, $\mathcal{H}_C$ would include at least one PL where it couples to the $i/o$ leads. Additionally, when non-orthogonal basis sets, such as those employed in LCAO, form the $\mathcal{H}_i$, $\mathcal{H}_o$, and $\mathcal{H}_C$ matrices, the coupling matrices $\mathcal{S}_i$, $\mathcal{S}_o$, and $\mathcal{S}_C$ should be provided. It is necessary to ensure that the system is isolated and large enough for sensing to be performed within the $input - C - output$ regions due to the electrostatic potential. By using a LCAO basis in our DFT calculations, the GPAW code uses the complete LCAO Hamiltonian of the full system within

the unit cell, which is useful for NEGF calculations. More details about this implementation are provided in Ref. 81.

Considering the NEGF-DFT framework, to obtain a spatial understanding of the path followed by the tunneling electron, the proper transmission channels establish it in the form of a decaying wave function. These are the best way to represent the closest path to the proper state in charge of conducting the electric current. The shape of these channels is energy dependent, generally taking the shape of the energetically closest molecular orbitals. They are also affected by the transfer capacity of the molecule, for example, the wave function decreases between atoms and molecules, the chemical potential and the hopping force. To some extent, the contribution of each orbital is related to the product of the orbital coefficients on the atoms at each terminal and is inversely proportional to the energy gap between the orbital and the Fermi energy, $\varepsilon_F$[83,84]. Thus, eigenchannels establish a pathway for differentiating between $\sigma$ and $\pi$ molecular bonds and anti-bonding orbitals, both of which are necessary for ET.

The efficiency of the DFT-NEGF method to model ET depends on the functional of correlation and exchange (xc) used as of the molecule in the central region itself. Unlike other computational methods to perform ET calculations, the DFT-NEGF method is emerging as the most practical and effective when considering computational capacity and time consumption[85,86]. A more general comparison of NEGF-DFT with LCAO is provided in Ref. 79.

## 2.10   Percolation Theory

In statistical physics and mathematics Percolation Theory describes the behavior of a network as the number of connections in the network increases. As described by Grimmett[87], percolation theory is the simplest model used to describe the statistical dependence of the disorder of a medium as additional connections are added. These may be dived into two main types of percolation: site percolation and bond percolation. In this work we will focus on the bond percolation and its mathematical model, as it provides the best description of the conduction process within a PVA/SWCNT CPC.

### 2.10.1  Bond Percolation

Bond percolation is a model that describes a regular point lattice $\mathbb{Z} = \mathbb{Z}^d$ in a Euclidean $d$-dimensional space which considers the edges of the lattice as the most relevant, as depicted schematically in Fig. 2.3).
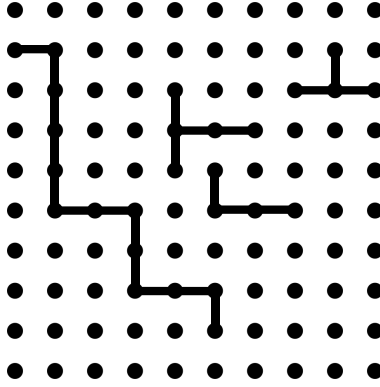


Figure 2.3:  Bond percolation representation.

The mathematical construction for bond percolation may be described in the following manner. First, we define the set $\mathbb{A} = \mathbb{A}^d$ of edges of $\mathbb{Z}$ to be the set

$$\mathbb{A} = \left\{ \{\mathbf{x}, \mathbf{y}\} : \mathbf{x}, \mathbf{y} \in \mathbb{Z}^d, |\mathbf{x} - \mathbf{y}| = 1 \right\}, \tag{2.60}$$

and designate each edge of $\mathbb{A}$ to be independently "open" with probability $P_{op} \in [0, 1]$ and closed with probability $P_{cl} = 1 - Popen$. Next, we define an open path to be any path in $\mathbb{Z}$ all of whose edges are open, and define the so-called open cluster $C(\mathbf{x})$ to be the connected component of the random sub-graph of $\mathbb{Z}$ consisting of only open edges and containing the vertex $\mathbf{x} \in \mathbb{Z}$. Write $C = C(\mathbf{0})$. The main objects of study in the bond percolation model are then the percolation probability $P_{perc}(P_{op}) = \mathbb{P}_p(|C| = \infty)$ and the critical probability $P_{crit} = \sup\{P_{op} : P_{perc}(P_{op}) = 0\}$, where $\mathbb{P}_p$ is defined to be the product measure $\mathbb{P}_p = \prod_{e \in \mathbb{A}^d} \mu_e$, $\mu_e$ is the Bernoulli measure

$$\mu_e = \left\{ \begin{array}{ll} P_{cl}, & \text{if } e \text{ is closed} \\ P_{op}, & \text{if } e \text{ is open} \end{array} \right. , \tag{2.61}$$

which assigns $P_{cl}$ whenever $e$ is closed and assigns $P_{op}$ whenever $e$ is open, and $P_{crit}$ is the percolation threshold. Bond models for which $P_{op} > P_{crit}$ will have fully connected components whereas those for which $P_{op} < P_{crit}$ will not.

In a thin film composed of SWCNTs embedded in a polymer matrix, e.g., PVA, there is a random distribution of the components, which can be considered as a complex network. For this reason it is important to consider the percolation theory, since PVA acts as an insulating "buffer" between the highly conductive SWCNTs, ensuring that the SWCNTs remain "debundled" and there is a minimum SWCNT$\cdots$SWCNT coverage threshold that allows the system to percolate.

There are models that use the percolation theory to determine the electrical conductivity in an insulating medium containing conductive media, similar to a PVA/SWCNT CPC. According to Mutlay and Tudoran[27], the conductivity of such systems follows a power law on of the following form

$$\sigma = \sigma_e \left( \phi - \phi_c \right)^s \tag{2.62}$$

where $\sigma$ is the conductivity, $\sigma_e$ is the effective conductivity, $\phi$ is the inclusion volume fraction, $\phi_c$ is the percolation threshold volume fraction, and $s$ is the critical exponent. Generally the magnitude of $s$ can range from one to three, i.e., $s \in [1, 3]$. In other words, the conductivity of (2.62) exhibits a linear to cubic dependence on the volume fraction difference from the percolation threshold.

## 2.11    Random Walk

Monte Carlo methods are a wide range of computational algorithms that focus on determining numerical outcomes from random samples. The underlying concept is to use randomness to solve problems that might be deterministic in principle. Random walk is one of the Monte Carlo methods that is useful to calculate the possible path that electrons could follow to go from the input lead to the output lead as shown in Fig. 2.4. If we consider a system similar to the one described in the previous section, in which an electron travels through a network full of connections, we cannot be sure of the exact path that said electron is traveling. However, we can say that the electron follows a random walk through the system until it reaches the other end and is measured. In order to calculate the conductivity of the system from the conductance, we need both the lead
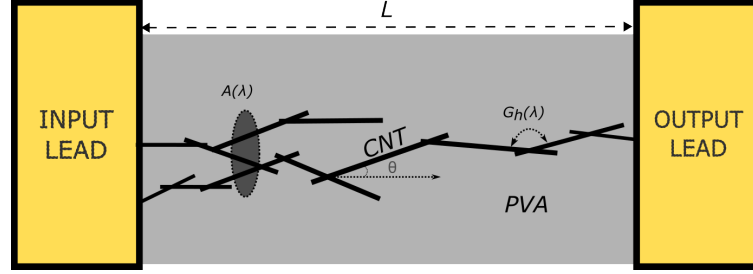
Figure 2.4:  Schematic representation of the conductance process of the studied system, bond percolation, cross sectional area, hopping conductance and zenithal angle $\theta$.

separation distance $L$ and the cross-sectional area in which an electron percolates $A$, where the latter may be treated as a random walk problem. Figure 2.4 provides a schematic representation of the conductance process of PVA/SWCNT system and the cross sectional area $A$.

According to Landau and Páez[88], assuming that a particle makes a number of steps $N$, the particle is equally likely to travel in any direction at each step. This means, the average radial distance travelled is

$$
\begin{aligned}
R^2 &= (\Delta x_1 + \Delta x_2 + \cdots + \Delta x_N)^2 + (\Delta y_1 + \Delta y_2 + \cdots + \Delta y_N)^2 \\
&= \Delta x_1^2 + \Delta x_2^2 + \cdots + \Delta x_N^2 + 2\Delta x_1 \Delta x_2 + 2\Delta x_1 \Delta x_3 + 2\Delta x_2 \Delta x_1 + \cdots \\
&\quad + \Delta y_1^2 + \Delta y_2^2 + \cdots + \Delta y_N^2 + 2\Delta y_1 \Delta y_2 + 2\Delta y_1 \Delta y_3 + 2\Delta y_2 \Delta y_1 + \cdots
\end{aligned}
\tag{2.63}
$$

If we take the average of a large number of such random steps, all the cross terms in (2.64) will tend to cancel and we will be left with

$$
\begin{aligned}
R_{\text{rms}}^2 &\simeq \left\langle \Delta x_1^2 + \Delta x_2^2 + \cdots + \Delta x_N^2 + \Delta y_1^2 + \Delta y_2^2 + \cdots + \Delta y_N^2 \right\rangle \\
&= \left\langle \Delta x_1^2 + \Delta y_1^2 \right\rangle + \left\langle \Delta x_2^2 + \Delta y_2^2 \right\rangle + \cdots \\
&= N \left\langle r^2 \right\rangle = N r_{\text{rms}}^2
\end{aligned}
\tag{2.64}
$$

$$
\Rightarrow R_{\text{rms}} \simeq \sqrt{N} r_{\text{rms}},
\tag{2.65}
$$

where $r_{\text{rms}} = \sqrt{\langle r^2 \rangle}$ is the root-mean-square step size.

## 2.12   Single-Walled Carbon Nanotube

Single-walled carbon nanotubes (SWCNTs) are formed by rolling a graphene sheet into a cylinder that typically has a diameter between 0.2 and 10.0 nm and a length between 0.1 $\mu m$ and 1 cm.[89] Because the length to diameter ratio ranges from one thousand to ten million, SWCNTs are considered one-dimensional objects.

Depending on the way the graphene sheet is rolled, SWCNTs can acquire different properties, among which we can differentiate achiral (zigzag or armchair) or chiral SWCNTs. To determine the type of SWCNTs, we need to define the chiral vector $\mathbf{C}_h$ which is directed along the circumference of the nanotube and is expressed in terms of the unit vectors $\mathbf{a}_1$ and $\mathbf{a}_2$ by

$$\mathbf{C}_h = n\mathbf{a}_1 + m\mathbf{a}_2 \equiv (n, m) \quad (0 \leq m \leq n), \tag{2.66}$$

where $n$ and $m$ are integers that determine the chiral angle $\theta = \arctan\left(\frac{\sqrt{3}n}{2m+n}\right)$. From here we can deduce that ($n = m, \theta = 30°$) corresponds to armchair SWCNTs, ($m = 0, \theta = 0°$) to zigzag SWCNTs, and other combinations ($0° < \theta < 30°$) to chiral SWCNTs as shown in Fig. 2.5.

In SWCNTs the electronic properties and band structure are affected by the periodicity of the carbon atoms. This is known as the zone folding approach and is derived from the tight junction model of graphene. For the development of this thesis, we only need to take into account the classification of the SWCNTs, which is established by the relationship of their indices: a SWCNT is metallic if $n - m \equiv 0$ mod 3, which includes all armchair-type SWNTs, otherwise it is semiconductor. If we consider curvature effects, the classification changes: armchair SWCNTs remain metallic, otherwise when indices $n - m \equiv 0$ mod 3, the nanotube has a finite space proportional to $1/d^2$ and $\sin 3\theta$ where $d$ is the diameter and $\theta$ is the chiral angle.[90]

The differences between metallic and semiconducting SWCNTs can be easily seen from their density of states (DOS). Metallic SWCNTs have non-zero DOS $\varrho(\varepsilon)$ near the Fermi level $\varepsilon_F$ ($\varrho(\varepsilon_F) \gg 0$), whereas for semiconducting nanotubes the DOS near the Fermi level is zero ($\varrho(\varepsilon_F) = 0$), as seen in Fig. 2.6. It can clearly be seen that DOS cannot be represented as a smooth function, but characteristic peaks can always be observed which are known as van Hove singularities. This feature of the DOS results from the one dimensional nature of SWCNTs. Each singularity is marked with the index of the valence ($v_1$, $v_2$) or conduction ($c_1$, $c_2$) sub-band to which it belongs in Fig. 2.6.
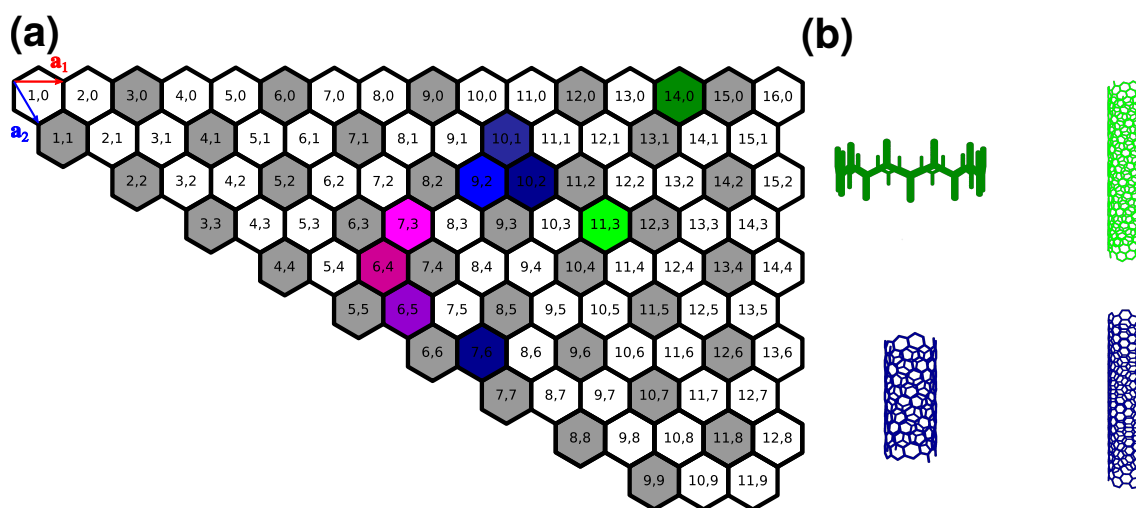
Figure 2.5: a) Graphene sheet showing the $a_1$ and $a_2$ vectors of equation (2.66) for zigzag (n,0), armchair (n,n), or chiral (n,m) SWCNTs and (b) prototypical atomic structures of zigzag (dark green) and chiral (green and blue) SWCNTs. Colored regions (excluding grey colors) shows the chirality of the SWCNTs that are present in the sample used to develop the experimental part.

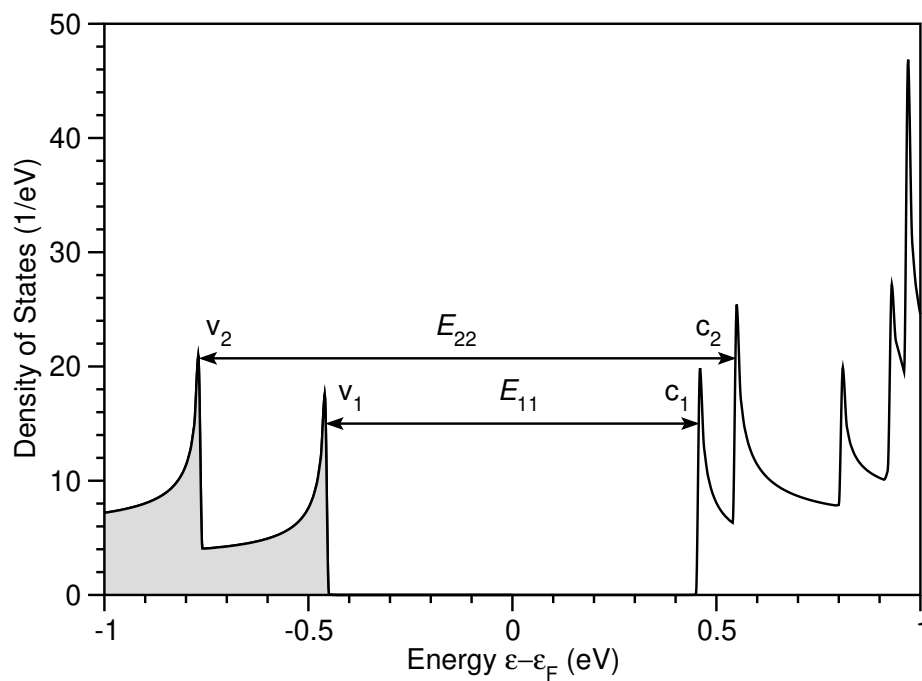Figure 2.6: Density of states in $eV^{-1}$ versus energy $\varepsilon$ relative to the Fermi level $\varepsilon_F$ in eV of a semiconducting (10,2) SWCNT. State occupation is marked in grey (valence band) and the arrows show the dominant $E_{11}$ and $E_{22}$ transitions.

# Chapter 3

# Methodology

## 3.1  Characterization of PVA/SWCNT thin films

The procedure for the fabrication of PVA/SWCNT CPC thin films and the results of the experimental measurements of the conductance are explained in the thesis of Jorge Suarez[91]. However, it is important to understand the characterization of the PVA/SWCNT composite since this will allow us to determine the chiralities of the SWCNTs and which is predominant at all stages of thin film processing.

One of the best experimental techniques to characterize carbon-based materials is Raman spectroscopy. Raman allows us to obtain characteristic peaks of SWCNTs, i.e., their radial breathing mode (RBM), and thus recognize their chirality, and concomitant electronic properties (semi-conductive or metallic nature). Moreover, Raman provides valuable information about defects in the structure, measuring the 2D and 3D values of the orientational order parameter and demonstrating the presence of any mechanical constraints at the SWCNTs surface due to changes in the micropolarities induced by pH changes, charge transfer, or the presence of other heavy macromolecules.

In our case, Raman was used to obtain a quantification of the orientational order parameter and to show the representative zones of the RBM. The Raman spectrum was obtained by exciting with a wavelength $\lambda_{ex}$ = 1064 nm both in the pure wet cake sample of SWCNTs, in solution with

the solvent, and within the PVA/SWCNT composite at different concentrations. For more details about the complete characterization of the PVA/SWCNT composite, we refer the reader to Refs. 91 and 92.

An important check of our computational procedure is to compare the experimental results. For this reason, RBM calculations were performed for the different SWCNTs that appear in the experimental sample.. This was accomplished using the ASE[93] and GPAW[94,95] libraries to realize DFT-based vibrational calculations. Using the ASE module, the Hessian and hence all modes of vibration for each SWCNT that appears in the measured Raman spectra were obtained and the vibrational mode corresponding to the RBM for each SWCNT was determined. Additionally, because the RBM frequency is inversely proportional to the diameter of the SWCNTs, we may approximate the SWCNTs' RBM using their calculated diameters in the formula

$$\omega_{\text{RBM}} = \frac{\alpha}{d} + \omega, \tag{3.1}$$

where $\alpha$ is the constant of proportionality between the RBM frequency and the inverse of the SWCNT's diameter, and $\omega_0$ is dependent on the SWCNT's physicochemical environment[96,97].

Once the predominant SWCNT chirality in the samples was established, the system to be modeled computationally was developed. Experimentally, the system consists of a CPC composed of PVA, with a molecular weight of each chain 440.52 g/mol and total molecular weight 85000 g/mol, and SWCNTs, with a molecular weight per unit cell of 248 carbon atoms or 2978.65 g/mol. However, due to the hydrophobic nature of the SWCNTs, a solvent is needed to make the composite with PVA. In our case the solvent is Brij-78, with a molecular weight of 1151.57 g/mol.

## 3.2   DFT Calculation Details

All total energies and atomic structures have been calculated using density functional theory (DFT). We employ a linear combination of atomic orbitals (LCAO) consisting of double-$\zeta$-polarized (DZP) basis sets, which is ideal for representing systems of several atoms per unit cell[58], to represent the Kohn-Sham wave functions and a real-space (RS) grid to represent the electron density within the projector augmented wave (PAW) method as implemented in the

GPAW software package. As described in Ref. 98, the generalized-gradient approximation (GGA) implementation of Perdew, Burke, and Ernzerhof (PBE) which has been employed throughout for the exchange and correlation (xc) functional with van der Waals (vdW) interactions included at the Grimme's D3 semi-empirical level (PBE-D3). All structures have been relaxed until a maximum force $F_{max} \leq 0.03$ $eV$/Å has been obtained, with a grid spacing of $h \approx 0.2$ Å and energies extrapolated to $T \rightarrow 0$. To avoid interactions between periodic images, we have employed more than 10 Å of vacuum perpendicular to the axis for SWCNT's[99] and PVA. We have also minimized the SWCNT's energy with respect to the cell length parallel to the SWCNT's axis, yielding a unit cell of $20.8 \times 20.8 \times 23.883$ Å$^3$ for the (10,2) SWCNT. PVA was modelled as an infinite chain consisting of ten PVA units with a relaxed unit cell of $25.4472 \times 16 \times 16$ Å$^3$.

To determine the ground state structure for PVA adsorbed on a SWCNT, we employ a non-orthogonal $25.4472 \times 33.07 \times 23.883$ Å$^3$ unit cell varying the angle $\gamma$ between $C_{20}O_{10}H_{40}$ chain and the SWCNT in the *xz*-plane from 30° to 90°. The SWCNT—$C_{20}O_{10}H_{40}$ separation was initially a short-range hydrogen bond configuration ($d_{OH\cdots C} \sim 1.8$ Å) and, after allowing the system to relax into its ground state configuration, yielded a long-range weak hydrogen bond ($d_{OH\cdots C} \sim 2.2$ Å) between PVA and the SWCNT. A similar procedure was employed to determine the ground state structure for a SWCNT adsorbed on a SWCNT, using a non-orthogonal $23.883 \times 33.07 \times 23.883$ Å$^3$ unit cell and varying the angle between the tubes in the *xz*-plane from 0° to 90°. These structures yielded a SWCNT—SWCNT separation of $d_{C\cdots C} \sim 3.4$ Å, consistent with the interlayer separation in graphite.

## 3.3   Modelling Adsorption

The binding energy, $E_{bind}$, of an adsorbate $X \in \{PVA, SWCNT\}$ on a given substrate $S \in \{SWCNT\}$ is obtained from the difference in energy between the separated and combined systems, so that

$$E_{bind}[X@S] \approx E[X] + E[S] - E[X@S]. \qquad (3.2)$$

Because we find PVA does not form covalent bonds with SWCNT we may safely neglect any difference in entropy between the adsorbed species. The ratio of forward to backward rate

constants for the adsorption process at room temperature, i.e. $25°C$, is then

$$K[X@S] \approx \exp\left(\frac{E_{bind}[X@S]}{k_B T}\right). \tag{3.3}$$

## 3.4 NEGF Calculation Details

The implementation of the Landauer-Bütticker formulation to determine the conductance in the system schematized in Fig. 2.2 was calculated using a multi-terminal implementation of the NEGF method. In this way, we can obtain the conductance between PVA-SWCNT and SWCNT-SWCNT. With this method, we obtain an excellent description of electronic transport. According to the method explained in Ref. 25, the multi-terminal procedure for NEGF can be calculated using the formula

$$G = G_0 \operatorname{Tr}\left[G_c \Gamma_{in} G_c^\dagger \Gamma_{out}\right]\Big|_{\epsilon=\epsilon_F} \tag{3.4}$$

where $G_c$ represents the Green's function in the central region of the junction and $\Gamma_{in/out}$ are the coupling to the semi-infinite input and output leads.

To describe the conductance process for the semiconducting system we have assumed that the SWCNTs are $p$-doped, due to common carbon vacancy defects in the SWCNT structure. This means that the Fermi energy $\epsilon_F$ should be taken as the energy of the valence-band maximum (VBM) $\epsilon_{VBM}$, and conductance occurs through the VBM.

## 3.5 Geometric Affine Deformation Model

To develop mathematical models of conductivity, the geometric affine deformation model for the PVA/SWCNT CPC first needs to be taken into account. The orientational order parameter $S$ for a uniaxially stretched SWCNT sample in 3D is defined as [100]

$$S = \frac{3\langle\cos^2\theta\rangle - 1}{2}, \tag{3.5}$$

by taking the statistical average of the angle $\theta$ between the SWCNT's axis and the direction of extension after stretching. Modelling the SWCNTs in the PVA film as rigid bodies undergoing

an affine deformation, this final zenithal angle $\theta$ may be expressed in terms of the initial zenithal angle $\theta_i$ and the ratio of final to initial extensions $\lambda = L_f/L_i$ of the sample as

$$\tan \theta = \lambda^{-3/2} \tan \theta_i \tag{3.6}$$

From (3.6), we can derive the following expressions for the sine and cosine functions of the zenithal angle $\theta$

$$\cos^2 \theta = \frac{\lambda^3}{\lambda^3 + \tan^2 \theta_i} \tag{3.7}$$

$$\sin^2 \theta = \frac{\tan^2 \theta_i}{\lambda^3 + \tan^2 \theta_i}, \tag{3.8}$$

as described in Appendix A.

Using (3.7) and (3.8) and assuming the nanotube orientations were initially uniformly distributed, so that the probability of having an initial zenithal angle $\theta_i$ is $P(\theta_i) = \sin \theta_i$, we may calculate the statistical average over $\theta$ of $\cos^2 \theta$ and $\sin^2 \theta$ as

$$\langle \cos^2 \theta \rangle = \int_0^{\frac{\pi}{2}} \frac{\lambda^3 \sin \theta_i d\theta_i}{\lambda^3 + \tan^2 \theta_i} = \frac{\lambda^3}{\lambda^3 - 1} \left( 1 - \frac{\arctan(\sqrt{\lambda^3 - 1})}{\sqrt{\lambda^3 - 1}} \right), \tag{3.9}$$

$$\langle \sin^2 \theta \rangle = \int_0^{\frac{\pi}{2}} \frac{\tan^2 \theta_i \sin \theta_i d\theta_i}{\lambda^3 + \tan^2 \theta_i} = \frac{\lambda^3}{\lambda^3 - 1} \left( \frac{\arctan \sqrt{\lambda^3 - 1}}{\sqrt{\lambda^3 - 1}} - \frac{1}{\lambda^3} \right). \tag{3.10}$$

Detailed derivations of (3.9) and (3.10) are provided in Appendicies A.1 and A.2, respectively.

Substituting (3.9) into (3.5), the definition of the orientational order parameter $S$, we obtain the geometric affine deformation model[100,101] $S_g$, which may be expressed more simply as

$$S_g = \frac{3}{2} \frac{\lambda^3}{\lambda^3 - 1} \left( 1 - \frac{\arctan(\sqrt{\lambda^3 - 1})}{\sqrt{\lambda^3 - 1}} \right) - \frac{1}{2}. \tag{3.11}$$

Similarly, using the geometric affine deformation model, we may calculate the average over $\theta$ of $\cos \theta$ and $\sin \theta$ as

$$\langle \cos \theta \rangle = \int_0^{\frac{\pi}{2}} \frac{\lambda^{3/2} \sin \theta_i}{\sqrt{\lambda^3 + \tan^2 \theta_i}} d\theta_i = \frac{\lambda^{3/2}}{\lambda^{3/2} + 1}, \tag{3.12}$$

$$\langle \sin \theta \rangle = \int_0^{\frac{\pi}{2}} \frac{\tan \theta_i \sin \theta_i}{\sqrt{\lambda^3 + \tan^2 \theta_i}} d\theta_i \approx \frac{1}{2} \frac{\sqrt{7\lambda + 3}}{\lambda^{3/2} + 1}. \tag{3.13}$$

Detailed derivations of (3.12) and (3.13) are provided in Appendicies A.3 and A.4, respectively.

# Chapter 4

# Results & Discussion

This chapter is divided into three main sections. In Section 4.1 the experimentally measured Raman spectra and conductance of thin films are discussed, in Section 4.2 the results of each of the theoretical models that were developed to obtain the conductivity are shown, and, finally, in Section 4.3 we compare our theoretical model to the experimental results together with the anisotropic analysis of the PVA/SWCNT composite.

## 4.1   Raman Spectra of the SWCNT Radial Breathing Mode

The results of the Raman spectrometry analyzes were obtained from three different samples. The first is a wet cake or paste that includes only the sample of SWCNTs as purchased. The second sample is a solution in the Brij-78 solvent of PVA and SWCNTs. The third is a sample thin film of the PVA/SWCNT composite.

In figure 4.1 the Raman spectrum (RBM region) of the first sample is shown together with a best fit that is its deconvolution into separate RBM modes of given SWCNTs. The spectrum was decomposed to show the contributions of each of the SWCNTs present in the sample. Among the SWCNTs that stand out the most are the (11,10), (14,0), (11,3), (9,4), (10.2), (7,6), (9,2), (6,5) and (7,3). The most intense RBM modes are those attributable to the (11,10), (10,2), (7,6) and (7,3) SWCNTs. It is important to mention that in the spectrum, the RBM of the (10,2) and (7,6)
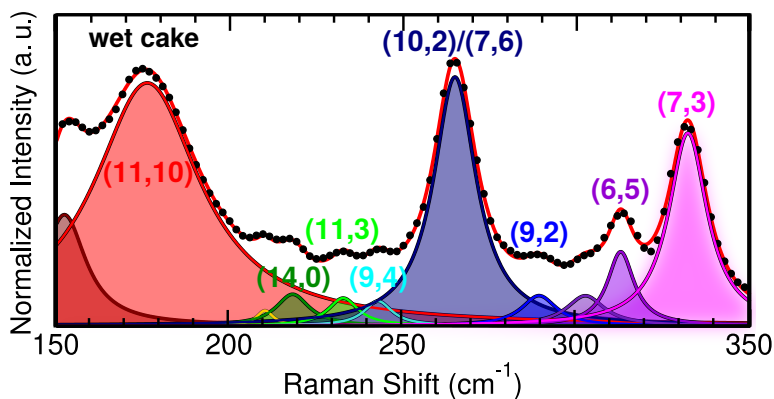
Figure 4.1: Raman Shift in $cm^{-1}$ of the RBM region for the as purchased pure pristine SWCNT wet cake sample.

SWCNTs are very similar, making it difficult to specify which is the SWCNT actually observed in the spectrum.
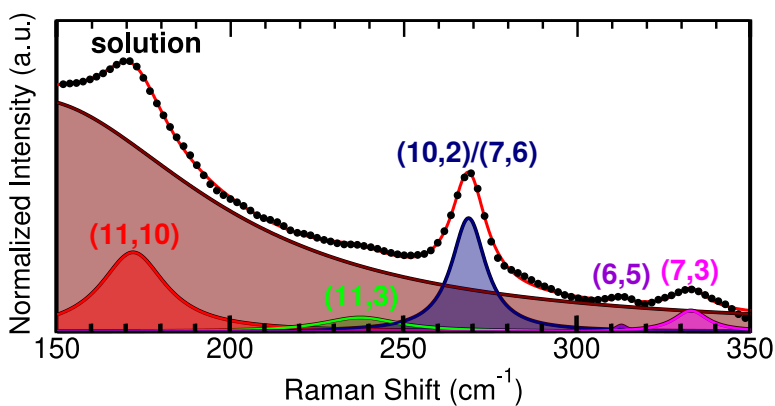


Figure 4.2: Raman Shift in $cm^{-1}$ of the RBM region for the Brij-78/PVA/SWCNT solution.

Figure 4.2 shows the RBM region of the Raman spectrum for the sample with solvent in solution. Again, the RBM of the SWCNTs can be clearly seen. In the same way as Fig. b4.1, the deconvolution of the spectrum is shown together with its decomposition to highlight the predominant SWCNTs in the solution. However, vibrational modes attributable to the sample being in solution "wash out" much of the SWCNTs' RBM modes, so that only the (11,10), (10,2), (7,6), (6,5), and (7,3) SWCNTs are clearly visible.
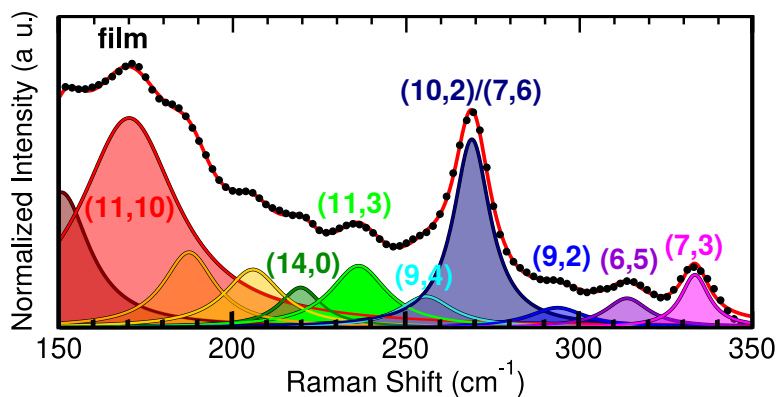
Figure 4.3: Raman Shift in in cm$^{-1}$ of the RBM region for the PVA/SWCNT thin film.

Finally, the spectrum of the dry composite between PVA/SWCNT is shown in Fig. 4.3. As in Figs. 4.1 and 4.2, the deconvolution and decomposition of the spectrum are shown. Figure 4.3 highlights the SWCNTs that are predominantmost common in the PVA/SWCNT thin film. Among these chiralities the (11,10), (10,2) and (7,6) again stand out. Based on this information, we can determine the SWCNTs that contribute the most to the conductance of the PVA/SWCNT system,

Table 4.1: Single-Walled Carbon Nanotube Chiral Indicies (**n, m**), Radial Breathing Modes $\omega_{RBM}$ in cm$^{-1}$ with $\lambda_{ex}$ = 1064 nm Excitation in Wet Cake, Solution, Film, from Ref. 102, and DFT Calculations, and DFT Calculated Diameter $d$ in Å.

| | radial breathing mode | | | | | diameter |
| | $\omega_{RBM}$ (cm$^{-1}$) | | | | | $d$ (Å) |
| chirality | wet cake | solution | film | ref. 102 | DFT | DFT |
|---|---|---|---|---|---|---|
| (7,3) | 332 | 333 | 333 | 330 | 321 | 7.11 |
| (6,5) | 313 | 313 | 314 | 311 | 305 | 7.63 |
| (9,2) | 289 | — | 294 | 295 | 282 | 8.10 |
| (7,6) | 265 | 269 | 269 | 267 | 255 | 8.98 |
| (10,2) | 265 | 269 | 269 | 267 | 256 | 8.87 |
| (11,3) | 233 | 237 | 236 | 233 | 221 | 10.17 |
| (14,0) | 218 | — | 219 | 215 | 202 | 11.38 |
| (11,10) | 176 | 172 | 170 | — | — | — |

and determine the most relevant SWCNT chirality to be simulated.

After obtaining the experimental RBM frequencies from the Raman spectrum, we calculate the same frequencies theoretically for the experimentally observed SWCNTs. The experimental and theoretical RBM frequencies are provided in  Table 4.1 and they are directly compared in
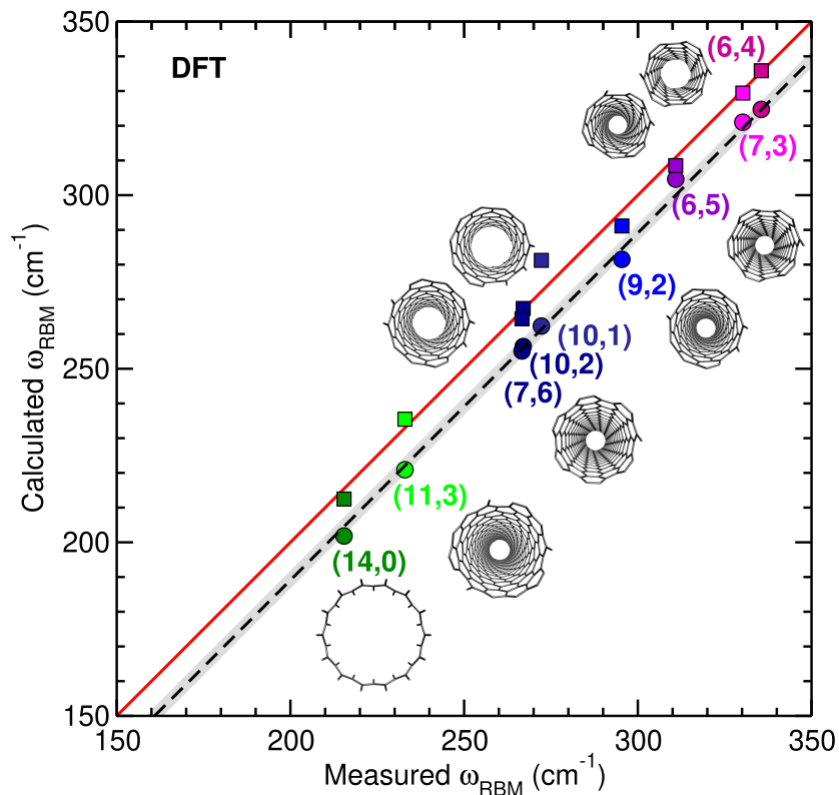


Figure 4.4:  Comparison between DFT and experimental calculations for RBM (filled colored circles), diameter (colored squares) and representation of each SWCNT chirality.

Fig. 4.4.  We observe a very good agreement between the experimental values for all samples, as well as with those calculated from DFT, up to a 11 cm$^{-1}$ mean absolute error. The observed minor underestimation of the RBM from DFT compared to the Raman measurements may be attributed to differences in the physiochemical environment, as all DFT calculations are performed in vacuum. Overall, these results clearly demonstrate the reliability of our DFT calculations for describing the SWCNTs in the PVA/SWCNT CPC.

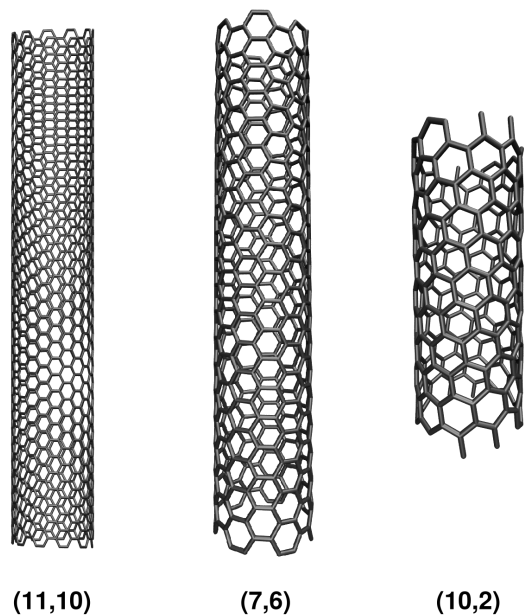**(11,10)**          **(7,6)**          **(10,2)**

Figure 4.5: Schematic representation of predominant SWCNTs in the thin film sample and comparison between their lengths.

Figure 4.5 shows the relaxed structures of the most prevalent SWCNTs in the PVA/SWCNT thin film. We can clearly see that the SWCNT with the fewest carbon atoms is the (10,2) SWCNT with 248 carbon atoms, while the others have 508 and 1324 carbon atoms for the (7,6) and (11,10) SWCNTs, respectively. For this reason, the (10,2) SWCNT has been chosen to simulate since having fewer atoms, the computational capacity required to perform NEGF conductance calculations will be less than with the others. However, as each SWCNT observed in the Raman spectra is semiconducting with similar diameters, differences between their conductivities are expected to be minor, so that our model can be applied to the measured SWCNT/PVA thin film.

Having chosen the SWCNT chirality to be simulated, conductance and adsorption energies were calculated as described in Chapter 3. As mentioned previously, SWCNTs are ballistic conductors. For this reason, conductance calculations have been performed in a unit cell containing a SWCNT···SWCNT junction, as depicted in Fig. 2.2.

On the one hand, the adsorption energies between SWCNTs are calculated depending on
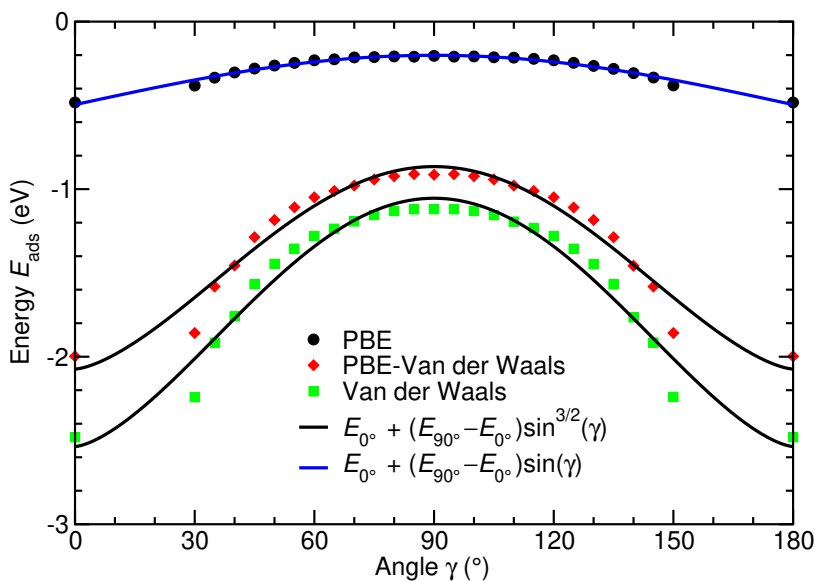
Figure 4.6: Adsorption energy versus the angle between the SWCNTs calculated using the PBE xc functional (filled black dots), including Van der Waals interactions at the Grimme's D3 (PBE-D3) level (filled green squares) and their difference (filled red diamond). Fits of the form $E_{0°} + (E_{90°} - E_{0°}) \sin \gamma$ (blue line) and $E_{0°} + (E_{90°} - E_{0°}) \sin^{3/2} \gamma$ (black lines) are also shown.

the angle between them $\gamma$. These energies are shown in Fig. 4.6 calculated using the PBE xc functional, including Van der Waals interactions between carbon atoms at the Grimme's D3 level (PBE-D3), and the difference between them, each with its own fit line. In figure 4.6, it can be clearly seen how there is a lower energy value when the SWCNTs are aligned both at 0° and at 180°, which indicates that the SWCNTs have a tendency (they would prefer) to "bundle", i.e., remain aligned with each other, as they would be in a lower energy state. However, it is important to mention that the experimental treatment performed to put the SWCNTs in solution was specifically made to "debundle", i.e., separate them, and prevent them from "rebundling".

On the other hand, we also perform calculations of the intertube transport conductance as a function of the SWCNT$\cdots$SWCNT angle $\gamma$, as shown in Fig. 4.7. The calculations were performed using two types of basis sets: single-$\zeta$-polarized and double-$\zeta$-polarized. As we see, there is no significant difference between calculations with either base set. In this way, we can justify that the calculated conductance is well converged with respect to basis set. In addition,

we can observe the change of conductance with respect to the angle between SWCNTs, having a higher conductance when the SWCNTs are aligned (0° and 180°), while conductance is shown to be lower for $\gamma = 75°$ or 105°.



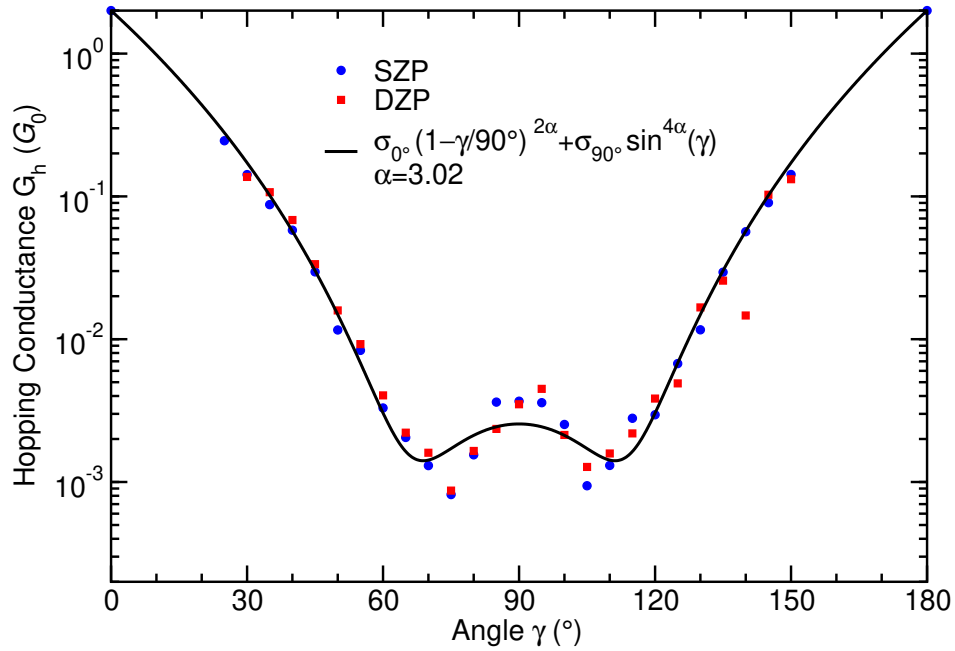Figure 4.7: Intertube transport conductance in units of the quantum of conductance $G_0$a (10,2) SWCNT junction, shown schematically in Fig. 2.2, as a function of the angle between the SWCNTs calculated using SZP (filled blue dots) and DZP (filled red squares) basis sets. The best fit of the form $\sigma_{0°}(1 - \gamma/90°)^{2\alpha} + \sigma_{90°} \sin^{4\alpha} \gamma$ (black line) is also provided.

## 4.2   Conductivity Models

In addition to simulating the components of the PVA/SWCNT CPC, we also focused on developing a mathematical model that explains the variation of the conductivity of the PVA/SWCNT composite. Our intention is that such a model can be used to describe the conductance of any polymer-based composite with SWCNTs. To develop the model, many considerations of what may affect the system were need to be made until the final model was obtained. Next, the different considerations that were made will be described and our reasons for rejecting or accepting a model will be explained.

**Model 1**

Since the definition of conductivity is related to conductance, we start by expressing the conductance of the a channel inside the system in terms of the number of "hops" between SWCNTs $N_h$, the distance the electrons travel through the film $L$, the "hopping" resistance $R_h$, which is described by the resistance the electron feels to passing through the separation between SWCNTs at each adsorption site, the zenithal angle $\theta$ and the distance between hops in the $n^{th}$ tube $\ell_n$ as

$$G_{ch} = \left[ \sum_{n=1}^{N} R_h(\gamma_n) \right]^{-1} = \frac{1}{N} \left[ \langle R_h(\gamma) \rangle_\gamma \right]^{-1} \tag{4.1}$$

$$= \frac{1}{L} \sum_{n=1}^{N} \frac{\ell_n \cos(\theta_n)}{N} \left[ \langle R_h(\gamma(\phi, \theta, \theta')) \rangle_{\phi,\theta,\theta'} \right]^{-1} \tag{4.2}$$

$$= \frac{\langle \ell \rangle_\ell \langle \cos \theta \rangle_\theta}{L} \left[ \langle R_h(\gamma(\phi, \theta_i, \theta_i', \lambda)) \rangle_{\phi,\theta_i,\theta_i'} \right]^{-1} \tag{4.3}$$

$$= \frac{\langle \ell \rangle}{L} \frac{\lambda^3}{\lambda^3 - 1} \left( 1 - \frac{1}{\lambda^{3/2}} \right) \left[ \langle R_h(\gamma(\phi, \theta_i, \theta_i', \lambda)) \rangle_{\phi,\theta_i,\theta_i'} \right]^{-1} \tag{4.4}$$

$$= \frac{\langle \ell \rangle}{L} \frac{\lambda^3}{\lambda^3 - 1} \left( 1 - \frac{1}{\lambda^{3/2}} \right) [\langle R_h(\lambda) \rangle]^{-1} \tag{4.5}$$

where the hopping resistance as a function of the SWCNT$\cdots$SWCNT angle $\gamma$ takes the form (*cf.* Fig. 4.7)

$$R_h(\gamma) \approx \sigma_{0°}(1 - \gamma/90°)^{2\alpha} + \sigma_{90°} \sin^{4\alpha} \gamma, \tag{4.6}$$

where $\alpha \approx 3.02$, $\sigma_{0°} \approx 2\ G_0$, and $\sigma_{90°} \approx 0.00255\ G_0$.

Assuming that the azimuthal angle $\phi$ does not change as the film is stretched, so that $\phi = \phi_i$, the average hopping resistance satisfies

$$\langle R_h\left(\gamma(\phi, \theta_i, \theta_i', \lambda)\right)\rangle_{\phi_i, \theta_i, \theta_i'} = \int_0^{2\pi} d\phi \int_0^{\pi/2} d\theta_i \int_0^{\pi/2} d\theta_i' \sin\theta_i \sin\theta_i' R_h\left(\gamma(\phi_i, \theta_i, \theta_i', \lambda)\right), \qquad (4.7)$$

where the SWCNT$\cdots$SWCNT angle $\gamma$ satisfies

$$\cos\gamma = \cos\phi \sin\theta \sin\theta' + \cos\theta \cos\theta' \qquad (4.8)$$

Using the geometric affine deformation model, as derived in Appendix A, we find

$$\cos\gamma = \frac{\cos\phi \sin\theta_i \sin\theta_i' + \lambda^3}{\sqrt{\lambda^3 + \tan^2\theta_i}\ \sqrt{\lambda^3 + \tan^2\theta_i}}. \qquad (4.9)$$

If we substitute (4.9) in (4.7) we can see that we will have an integral that is too complicated to solve analytically, so we will solve it numerically.

We may model the average distance between hops $\langle \ell \rangle$ in terms of the average total SWCNT length $\ell_0$, and the number of SWCNT junctions per tube $N_{\mathrm{CNT}}$ as

$$\langle \ell \rangle = \ell_0 \left(1 - \frac{2}{\max(2, N_{\mathrm{CNT}}) + 1}\right) \min\left\{1, \frac{N_{\mathrm{CNT}}}{2}\right\} \qquad (4.10)$$

where $N_{\mathrm{CNT}} = n_s \Theta_{\mathrm{CNT}}$ is the number of SWCNTs adsorbed on each SWCNT, $n_s = \ell_0/u_{\mathrm{CNT}}$ is the number of available sites for adsorption on a SWCNT, $\ell_0 \approx 500$ nm is the average total length of a SWCNT, $u_{\mathrm{CNT}} \approx 2.4$ nm is the unit cell length, and $\Theta_{\mathrm{CNT}}$ is the fractional coverage by SWCNTs $\Theta_{\mathrm{CNT}}$. The latter may be described by

$$\Theta_{\mathrm{CNT}} \approx \frac{C_{\mathrm{CNT}} K_{\mathrm{CNT}}}{1 + C_{\mathrm{CNT}} K_{\mathrm{CNT}} + C_{\mathrm{PVA}} K_{\mathrm{PVA}}}, \qquad (4.11)$$

where $C_{\mathrm{CNT}}$ and $C_{\mathrm{PVA}}$ are the fractional concentrations of CNTs and PVA in solution, respectively, and $K_{\mathrm{CNT}}$ and $K_{\mathrm{PVA}}$ are the ratios of forward to backward rate constants for the adsorption of CNTs and PVA on a CNT, respectively, i.e.,

$$K = \frac{k_+}{k_-} \approx \exp\left(\frac{E_{\mathrm{bind}}}{k_B T}\right) \qquad (4.12)$$

where $E_{\mathrm{bind}}$ is the binding energy and $k_B T \approx 25$ meV at room temperature. For SWCNT we find $E_{\mathrm{bind}}[\mathrm{CNT}] \approx 0.483$ eV whereas for a PVA $E_{\mathrm{bind}}[\mathrm{PVA}] \approx 0.446$ eV. Here we have assumed that the adsorption reaction does not significantly reduce the entropy of the adsorbed molecule, i.e., $\Delta S \approx 0$, since the molecules are physisorbed rather than chemisorbed. The total conductance $G_{\mathrm{tot}}$ of the film is then

$$G_{\mathrm{tot}} = \sum_n^{N_{ch}} G_{ch} = N_{ch} \langle G_{ch} \rangle \approx \frac{c_{\mathrm{CNT}} A L}{N} \langle G_{ch} \rangle \tag{4.13}$$

$$= \frac{c_{\mathrm{CNT}} A \langle \ell \rangle^2}{L} \left( \frac{\lambda^3 (1 - \lambda^{-3/2})}{\lambda^3 - 1} \right)^2 \frac{1}{\langle R_h(\lambda) \rangle} \tag{4.14}$$

where $c_{\mathrm{CNT}}$ is the concentration of CNTs in the dried film in molecules per unit volume, $A$ is the cross-sectional area of the film, $N_{ch}$ is the number of channels, and $N$ is the number of SWCNTs per channel. The total conductivity of the sample $\sigma_{\mathrm{tot}} = \frac{L}{A} G_{tot}$ is then

$$\sigma_{\mathrm{tot}} = \frac{c_{\mathrm{CNT}} \langle \ell \rangle^2}{\langle R_h(\lambda) \rangle} \left( \frac{\lambda^3 (1 - \lambda^{-3/2})}{\lambda^3 - 1} \right)^2 \tag{4.15}$$

$$\sigma_{\mathrm{tot}} = \frac{c_{\mathrm{CNT}} \ell_0^2}{\langle R_h(\lambda) \rangle} \left( \frac{\lambda^3 (1 - \lambda^{-3/2})}{\lambda^3 - 1} \right)^2 \left( 1 - \frac{2}{\min(2, N_h) + 1} \right)^2 \max \left\{ 1, \frac{N_h}{2} \right\}^2 \tag{4.16}$$

where $c_{\mathrm{CNT}}$ is given by

$$c_{\mathrm{CNT}} = \frac{N_A}{\mu_{\mathrm{CNT}}} \frac{M_{\mathrm{CNT}}}{V(\lambda)} = \frac{N_A u_{\mathrm{CNT}}}{\mu_{\mathrm{C}} n_{\mathrm{C}} \ell_0} \frac{M_{\mathrm{CNT}} h}{\pi r^2 \lambda h^2(\lambda)} \approx 1.22 \times 10^{17} \frac{\rho_{\mathrm{CNT}} h}{\lambda h^2(\lambda)}. \tag{4.17}$$

Here, $c_{\mathrm{CNT}}$ is the SWCNT concentration in molecules per mL where $N_A$ is Avogadro's number, $\mu_{\mathrm{CNT}}$ is the molar mass of the CNTs, $M_{\mathrm{CNT}} \approx 8\rho_{\mathrm{CNT}}$ g is the mass of CNTs in the sample, $V(\lambda) = \pi r^2 h \rho(\lambda) \approx \pi r^2 \lambda h^2(\lambda)/h \approx 0.827 \lambda h^2(\lambda)/h^2$ mL is the volume after stretching, $\mu_{\mathrm{C}} = 12.0107\mu$ is the molar mass of C atoms, $n_C \approx 248$ is the number of C atoms per unit cell in the CNT, $\ell_0 \approx 500$ nm is the length of the CNTs, and $u_{\mathrm{CNT}} \approx 2.4$ nm is the distance between CNT adsorption sites.

With the model described, we may proceed to calculate the conductivity of the system numerically as a function of the SWCNT concentration in the PVA/SWCNT CPC and the extension ratio $\lambda$. However, this model grossly overestimates the PVA/SWCNT composite's conductivity as compared to the experimental measurements. This is because (4.17) considers that every SWCNT

contributes to the conductivity of the system. However, depending on the number of SWCNTs adsorbed in a channel, only a portion of them may contribute to conductivity since electricity follows the path of least resistance. To correct for this overestimation of the fraction of SWCNTs that contribute to the conductivity of the PVA/SWCNT CPC, we must consider the percollation path and its cross-sectional area.

**Model 2**

We may reduce the conductivity by considering the probability that SWCNTs form a junction depending on their concentration in the CPC. In this way, the probability that two or more SWCNTs are adsorbed should be taken into account. Additionally, percolation theory, as discussed in Section 2.10 of Chapter 2, is used considering a percolation threshold of two. This means that to have conductivity in the system, there must be at least two adsorbed SWCNTs, on average, to form a conductance channel for electrons, also defined as the connectivity of the system. Finally, with these changes to the mathematical model for conductivity, we obtain

$$\sigma_{ch} = \frac{L}{A(\lambda)} \frac{P_{\geq 2}(N_{CNT}) C_{ch}(N_{CNT})}{N_h(N_{CNT}, \lambda)} \langle G_h(\lambda) \rangle, \tag{4.18}$$

where $L$ is the separation between the leads, $A(\lambda)$ is the extension dependent cross sectional area of the channel, $N_h$ is the number of hops between SWCNTs in the channel, $N_{CNT} = n_S \Theta_{CNT}$ is the average number of SWCNTs adsorbed on a SWCNT, $P_{\geq 2}(N_{CNT})$ is the probability of having more than two adsorbed SWCNTs, $C_{ch}(N_{CNT})$ is the connectivity of the channel, and $\langle G_h(\lambda) \rangle$ is the average intertube hopping conductance between two SWCNTs.

The probability of a SWCNT being connected is then

$$P_{\geq 2}(\Theta_{CNT}) = 1 - (1 + n_s \Theta_{CNT} - \Theta_{CNT}) (1 - \Theta_{CNT})^{n_S - 1}. \tag{4.19}$$

The connectivity of the channel may be expressed as a power law of the form[87]

$$C_{ch}(N_{CNT}) = (N_{CNT} - 2)^s, \tag{4.20}$$

where the exponent satisfies $1 \lesssim s \lesssim 3$,[17] as discussed in Section 2.10. In this way, we account for the contribution from multiple connections within the channel to its conductance,

with $N_{CNT} = 2$ at the percolation threshold of the network. The number of hops satisfies

$$N_h(N_{CNT}, \lambda) = \frac{L}{\langle \ell \cos\theta \rangle} = \frac{L}{\ell_0} \frac{N_{CNT} + 1}{N_{CNT} - 1} \frac{\lambda^{3/2} + 1}{\lambda^{3/2}}, \tag{4.21}$$

where $\ell$ is the distance between hops along the CNT, and $\ell_0$ is the CNT's total length. Substituting (4.20) and (4.21) into (4.18) we find

$$\sigma_{ch} = \frac{\ell_0}{A(\lambda)} \frac{N_{CNT} - 1}{N_{CNT} + 1} \frac{\lambda^{3/2}(N_{CNT} - 2)^t}{\lambda^{3/2} + 1} P_{\geq 2}(N_{CNT}) \langle G_h(\lambda) \rangle. \tag{4.22}$$

The cross-sectional area of the channel may be described as

$$A(\lambda) = A_0 \langle \sin^2\theta \rangle = \frac{\pi \ell_0^2 N_h(N_{CNT}, \lambda)}{\lambda^3 - 1} \left( \frac{\lambda^3 \arctan\sqrt{\lambda^3 - 1}}{\sqrt{\lambda^3 - 1}} - 1 \right), \tag{4.23}$$

where $A_0$ is the initial cross-sectional area. Assuming the individual CNTs are randomly oriented, we find the encompassed cross sectional area may be described as a random walk, i.e., $A_0 \approx \pi N_h(N_{CNT}, \lambda) \ell_0^2$. Substituting (4.23) into (4.22), we obtain

$$\sigma_{ch} = \frac{\lambda^3}{\pi L} \frac{\lambda^{3/2} - 1}{\lambda^{3/2} + 1} \left( \frac{N_{CNT} - 1}{N_{CNT} + 1} \right)^2 \frac{(N_{CNT} - 2)^t P_{\geq 2}(N_{CNT})}{\lambda^3 \frac{\arctan\sqrt{\lambda^3 - 1}}{\sqrt{\lambda^3 - 1}} - 1} \langle G_h(\lambda) \rangle. \tag{4.24}$$

Finally, we will approximate the average length of the SWCNTs in the PVA/SWCNT CPC using a TEM image obtained from Ref. 103. Their SWCNT sample underwent a similar treatment to that employed in our experiments (see Fig. 4.8). However, it is necessary to highlight that it is not the same method of preparation of the SWCNTs used in this work, and the final result for the average length may be slightly different.

As can be seen in Fig. 4.8, none of the SWCNTs are completely within the dimensions of the image. For this reason, the binomial distribution of the measured lengths does not describe the actual SWCNTs' lengths, because the SWCNTs may be much longer than what can be observed.

To solve this problem, we may analyze the image using Monte Carlo[88] methods. A typical Monte Carlo-type problem in computational physics is to try to determine the area of an arbitrarily shaped lake within a field of the known area only by throwing rocks. Here, the fraction of rocks thrown that fall in the lake is the ratio of the lake's area to the encompassing area of the field. If
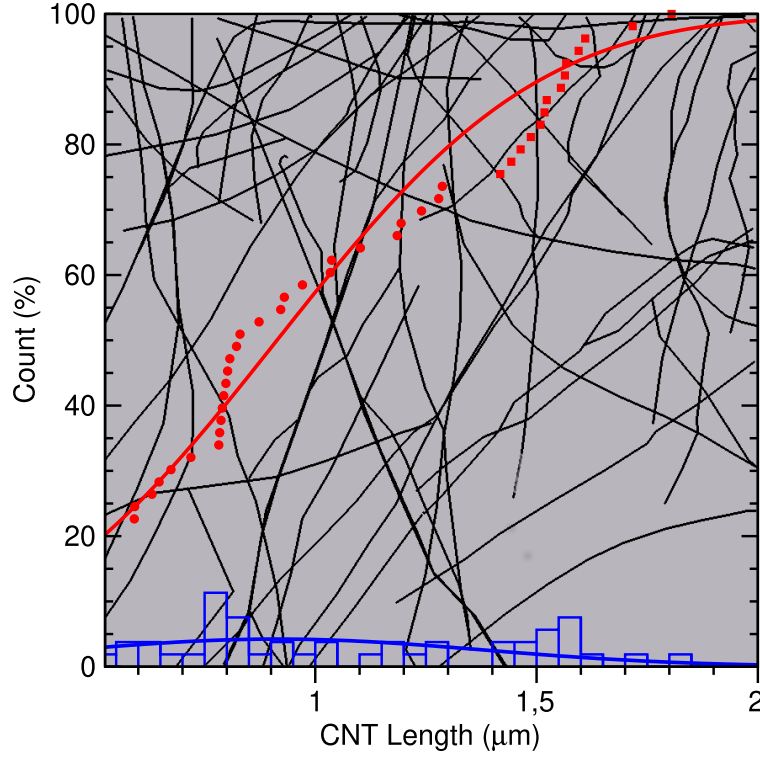
Figure 4.8: Statistical analysis of SWCNT lengths $\ell$ in μm extracted from TEM micrograph of Ref. 103 (gray background). Measured count % and SWCNT length (red filled circles) obtained, and minimum length for SWCNTs which pass over the edge of the image (red filled squares) are provided with their best fit cummulative distribution function $\frac{1}{2}\left[1 + \mathrm{erf}\left(\frac{\ell - \langle\ell\rangle}{\sigma}\right)\right]$ (red solid line and filled region), where $\langle\ell\rangle \approx 0.91$, $\sigma \approx 0.47$ μm, and resulting histogram and Gaussian distribution (blue solid line).

we assume that the rocks are the ends of each SWCNT and the area to be determined is the length of the SWCNTs, then the same method can be applied.

The fraction of SWCNTs in an $L \times L$ TEM micrograph including an end, $P_{\mathrm{end}}$, may be described by

$$P_{\mathrm{end}} = \frac{2}{\pi} \int_0^{\frac{\pi}{2}} d\vartheta \int_0^{\ell_0} \frac{d\ell}{\ell_0} \int_0^L \frac{dx_0}{L} \Theta\left(L - x_0 - \ell\cos\vartheta\right) \Theta\left(L - \ell\sin\vartheta\right), \qquad (4.25)$$

where $\Theta(x) = \begin{cases} 1, & x \geq 0 \\ 0, & x < 0 \end{cases}$ is the Heaviside step function and $\ell_0$ is the length of the SWCNT. Here, the probability is averaged over the SWCNT's polar angle $\vartheta$, its length $\ell$ inside the image, and the position $x_0$ where it crosses the $x$-axis.

Evaluating (4.25) we obtain

$$P_{\text{end}} = \frac{2}{\pi} \int_0^{\frac{\pi}{2}} d\vartheta \left[ \frac{\ell}{\ell_0} - \frac{\ell^2}{2L\ell_0} \cos \vartheta \right]_0^{\min\left\{ \ell_0, \frac{L}{\sin \vartheta}, \frac{L}{\cos \vartheta} \right\}}$$

$$= \frac{\pi - 4\cos^{-1} \frac{1}{\bar{\varrho}} + \sqrt{\bar{\varrho}^2 - 1} - \frac{\varrho}{\varrho_{>1}}}{\pi} + \frac{3 \ln \left( \bar{\varrho} + \sqrt{\bar{\varrho}^2 - 1} \right) + 1 - \bar{\varrho}}{\pi \varrho}. \tag{4.26}$$

where $\varrho \equiv \ell_0 / L$ is the ratio of CNT to image length, $\varrho_{>1} \equiv \max\{\varrho, 1\}$, and $\bar{\varrho} \equiv \min\{\varrho_{>1}, \sqrt{2}\}$. Considering separately (4.26) on the ranges $\varrho \leq 1$, $1 \leq \varrho \leq \sqrt{2}$, and $\varrho \geq \sqrt{2}$, we find

$$P_{\text{end}} = \begin{cases} 1 - \frac{1}{\pi} \varrho, & \varrho \leq 1 \\ 1 - \frac{4}{\pi} \cos^{-1} \frac{1}{\varrho} + \frac{\sqrt{\rho^2 - 1} - 2}{\pi} + \frac{3 \ln \left( \varrho + \sqrt{\varrho^2 - 1} \right) + 1}{\pi \varrho}, & 1 \leq \varrho \leq \sqrt{2} \\ \frac{3 \ln \left( 1 + \sqrt{2} \right) + 1 - \sqrt{2}}{\pi \varrho}, & \varrho \geq \sqrt{2} \end{cases} \tag{4.27}$$

From (4.27) we see that $P_{\text{end}}$ decreases linearly from 1 to $1 - \frac{1}{\pi} \approx 0.6817 \sim \text{2/3}$ as the CNT length increases from 0 to $L$, and decreases inversely from $\frac{3 \ln(1 + \sqrt{2}) + 1 - \sqrt{2}}{\pi \sqrt{2}} \approx 0.5019 \sim \text{1/2}$ for $\varrho \geq \sqrt{2}L$. In this way we may easily estimate the average length of the CNTs in the sample from the fraction of CNTs in the micrograph which display an end, $f_{\text{end}}$, using $\ell_0 \approx \pi(1 - f_{\text{end}})L$ when $f_{\text{end}} > \text{2/3}$, and using $\ell_0 = \frac{3 \ln(1 + \sqrt{2}) + 1 - \sqrt{2}}{\pi} \frac{L}{f_{\text{end}}} \approx 0.71 L / f_{\text{end}}$ when $f_{\text{end}} < \text{1/2}$.

Using (4.27) on the data provided by the TEM image, we find the average length of the SWCNTs is approximately 2.7 $\mu$m, which is a much larger value than that estimated by the TEM image. In Fig. 4.9 we see the approximate lengths for the complete CNT image and also the approximate lengths if we divide the image into four equal parts. All this is in order to establish an average value between all the measurements since we only have one image that is available for analysis.

The final result of this new model showed a significant decrease in the conductivity of the system. However, significant discrepancies are still present in the experimental results. This is
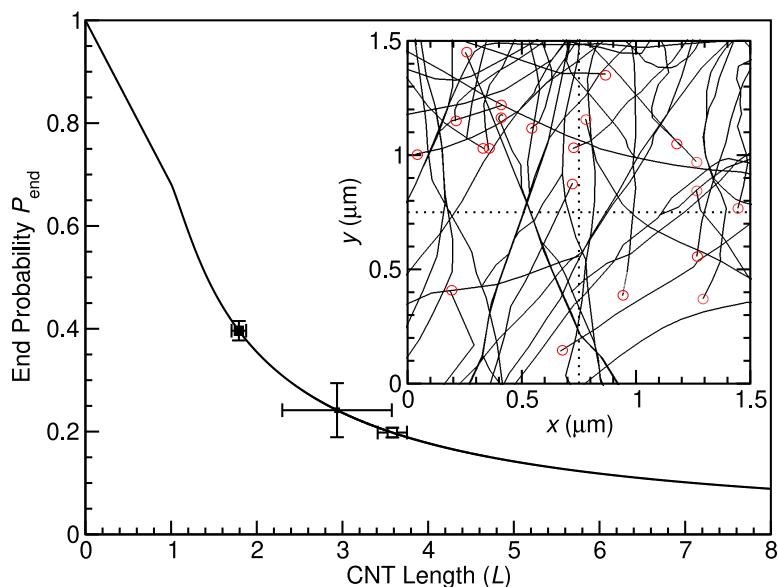
Figure 4.9: Probability of a CNT in an $L \times L$ micrograph displaying at least one end, $P_{end}$, versus the CNT's length $\ell_0$ in units of $L$. An analysis of a prototypical $1.5 \times 1.5$ μm$^2$ TEM micrograph from Ref. 103 is provided as an inset, with all CNT ends within the micrograph marked (red circles). The fraction of CNTs displaying an end and the estimated CNT length for the entire (filled large square) and a quarter (filled small square) of the image, along with the estimate for a quarter based on the entire image (black empty square).

because the exponent of the connectivity dominates the conductivity, and the probability of having more than two adsorbed SWCNTs is practically 100% for the SWCNT concentrations used and the average of the conductance of the channel increases its value with increasing concentration. To address these issues, we should include both the waviness of the SWCNTs and include the influence of connectivity as a supplementary channel, with $s = 1$.

**Model 3**

Finally, we now simplify our model. We discard the factor of the probability of having two or more adsorbed SWCNTs, as this is considered explicitly via the connectivity. Moreover, for the average of the conductivity of the channel, we use the theoretical value obtained from the DFT

calculations for the most likely angle at which the SWCNTs are aligned. The conductivity for the angle of 90° ≈ 0.00255 $G_0$. In our case, we use the conductance value for $\gamma = 90°$, as the conductance has a rather flat behaviour in the most probable region. On the other hand, the value of the exponent $s$ used for system connectivity is one. The resulting conductance is given by

$$G_{ch} = \frac{N_{CNT} - 2}{N_h \langle R_h \rangle} \left( 1 + \frac{1/2 N_{CNT} - 1}{3u} \right),$$ (4.28)

where $N_{CNT}$ is the number of SWCNTs per tube to which hopping is possible, $N_h$ is the number of hops required to traverse the channel, $\langle R_h \rangle$ is the average resistance per hop, and $u$ is the SWCNTs' waviness, that is, the ratio of their total to effective length. Here $N_{CNT} \equiv s_{CNT} \Theta_{CNT}$, where $s_{CNT}$ is the number of sites where SWCNTs or PVA may physisorb on a tube, and $\Theta_{CNT}$ is the fractional coverage of a SWCNT by SWCNTs. In this way, the numerator of (4.28) describes the number of parallel paths available within the channel, that is, how much the SWCNT coverage is above the threshold for percolation of two SWCNTs per tube, with the Heaviside step function ensuring the conductance is zero when $N_{CNT}$ is below the percolation threshold. In contrast, the denominator of (4.28) describes the resistance of a single path consisting of $N_h$ hops in series, each with average resistance $\langle R_h \rangle$. Using (4.28) we may model the conductivity of a PVA/SWCNT thin film as

$$\sigma_{mod} = \frac{L}{A} G_{ch} = \frac{L}{A} \frac{(N_{CNT} - 2)}{N_h \langle R_h \rangle} \left( 1 + \frac{N_{CNT} - 2}{6u} \right),$$ (4.29)

where $L$ is the length of the conducting channel and $A$ is the channel's cross-sectional area. We may model this area as that encompassed by a set of randomly oriented hops, i.e., as a "random walk". This means the cross-sectional area is proportional to the number of hops $N_h$ and the average of the square of the distance between hops $\langle \ell^2 \rangle$. For a channel oriented in the direction of extension, this yields

$$A = \pi N_h \langle \ell^2 \sin^2 \theta \rangle = \frac{\pi N_h \langle \ell^2 \rangle}{\lambda^3 - 1} \left( \lambda^3 \frac{\arctan \sqrt{\lambda^3 - 1}}{\sqrt{\lambda^3 - 1}} - 1 \right),$$ (4.30)

where $\ell$ is the distance between hops onto and off of a SWCNT, and we describe $\langle \sin^2 \theta \rangle$ using the geometric affine deformation model via (3.8). Substituting (4.30) into (4.29), we find the conductivity parallel to the extension direction may be described by

$$\sigma_{mod}^{\parallel} = \frac{L}{\pi N_h^2 \langle \ell^2 \rangle} \frac{(\lambda^3 - 1)(N_{CNT} - 2)}{\lambda^3 \frac{\arctan \sqrt{\lambda^3 - 1}}{\sqrt{\lambda^3 - 1}} - 1} \frac{1 + \frac{N_{CNT} - 2}{6u}}{\langle R_h \rangle}.$$ (4.31)

The number of hops, $N_h$, required to traverse a distance $L$ is simply the ratio of $L$ to the average distance between hops in the conduction direction $\langle \ell \cos \theta \rangle$. This yields

$$N_h^2 = \frac{L^2}{\langle \ell \rangle^2 \langle \cos \theta \rangle^2} = \frac{L^2}{\langle \ell \rangle^2} \frac{(\lambda^{3/2} + 1)^2}{\lambda^3}, \tag{4.32}$$

where we have again described $\langle \cos \theta \rangle$ using the geometric affine deformation model via (3.9). Substituting (4.32) into (4.31), we find

$$\sigma^{\parallel}_{\text{mod}} = \frac{1}{\pi L_0} \frac{\langle \ell \rangle^2}{\langle \ell^2 \rangle} \frac{\lambda^{3/2} - 1}{\lambda^{3/2} + 1} \frac{\lambda^2 (N_{\text{CNT}} - 2)}{\lambda^3 \frac{\arctan \sqrt{\lambda^3 - 1}}{\sqrt{\lambda^3 - 1}} - 1} \frac{1 + \frac{N_{\text{CNT}} - 2}{6u}}{\langle R_h \rangle}, \tag{4.33}$$

where $L = L_0 \lambda$ when measuring the conductivity parallel to the extension direction. This is because every time the thin film is subjected to the stretching process, the initial length $L_0$ is affected by the factor $\lambda$.

| sample | wt.% in solution | | | wt.% dry content | | |
|---|---|---|---|---|---|---|
| | PVA | SWCNT | Brij 78 | PVA | SWCNT | Brij 78 |
| **A** | 10.00 | 0.05 | 1.00 | 90.50 | 0.45 | 9.05 |
| **B** | 10.00 | 0.10 | 1.00 | 90.09 | 0.90 | 9.01 |
| **C** | 10.00 | 0.20 | 1.00 | 89.29 | 1.79 | 8.93 |
| **D** | 10.00 | 0.30 | 1.00 | 88.50 | 2.65 | 8.85 |

Table 4.2: PVA/SWCNT CPC Sample Weight % (wt.%) of PVA, SWCNT, and Brij 78 in Solution and Dry Content.

Next, we evaluate the model taking into account the concentration values shown in Table 4.2 for dry content. The values for the extension ratio range from 1 to 5, the ratio value between $\langle \ell \rangle^2 / \langle \ell^2 \rangle = 2/3$ and the waviness $u = 1.11$. The latter means the effective length of a SWCNT is 90% of the actual length.

Finally, we establish a way to calculate the perpendicular conductivity of the sample in relation to the parallel conductivity as

$$\sigma^{\perp}_{\text{mod}} = \frac{\langle \sin \theta \rangle^2 \langle \cos \varphi \rangle^2}{1 - \langle \sin^2 \theta \rangle \langle \cos^2 \varphi \rangle} \frac{\langle \sin^2 \theta \rangle}{\langle \cos \theta \rangle^2} \sigma^{\parallel}_{\text{mod}}, \tag{4.34}$$

where $\varphi$ is the azimuthal angle in the *xy*-plane. However, $\varphi$ does not depend upon the extension in the *z*-direction, $\lambda$, so that $\langle \cos \varphi \rangle = 2/\pi$ and $\langle \cos^2 \varphi \rangle = 1/2$.

As a result, substituting (3.10) and (3.13) for $\langle \sin^2 \theta \rangle$ and $\langle \sin \theta \rangle$, respectively, we find

$$\sigma_{\text{mod}}^{\perp} = \frac{2\lambda^{3/2}}{\pi^3 L_0} \frac{\langle \ell \rangle^2}{\langle \ell^2 \rangle} \frac{\lambda^{3/2} - 1}{\lambda^{3/2} + 1} \frac{(7\lambda + 3)(N_{\text{CNT}} - 2)}{\lambda^3 - 1 + \lambda^3 \left(1 - \frac{\arctan \sqrt{\lambda^3 - 1}}{\sqrt{\lambda^3 - 1}}\right)} \frac{1 + \frac{N_{\text{CNT}} - 2}{6u}}{\langle R_h \rangle} \tag{4.35}$$

where $L = L_0 \lambda^{-3/2}$ when measuring the conductivity perpendicular to the extension direction. In contrast with the parallel case, perpendicular length is affected via a factor of $\lambda^{-3/2}$ as seen in the geometric affine deformation model (3.6).

To apply the conductivity models provided in (4.33) and (4.35), we require an estimate of the SWCNT's coverage by SWCNTs, $\Theta_{\text{CNT}}$, which is going to determine the number of SWCNTs adsorbed as

$$N_{\text{CNT}} = \Theta_{\text{CNT}} s_{\text{CNT}} \tag{4.36}$$

and $\Theta_{\text{CNT}}$ may be described using

$$\Theta_{\text{CNT}} \approx \frac{s_{\text{CNT}} C_{\text{CNT}} K_{\text{CNT}}}{1 + s_{\text{CNT}} C_{\text{CNT}} K_{\text{CNT}} + s_{\text{PVA}} C_{\text{PVA}} K_{\text{PVA}}}, \tag{4.37}$$

where $s_{\text{CNT}}$ and $s_{\text{PVA}}$ are the numbers of adsorption sites per SWCNT and PVA, respectively, $C_{\text{CNT}}$ and $C_{\text{PVA}}$ are the fractional concentrations of SWCNTs and PVA in solution, respectively, and $K_{\text{CNT}}$ and $K_{\text{PVA}}$ are the ratios of forward to backward rate constants for the adsorption of SWCNTs and PVA on a SWCNT, respectively, i.e.,

$$K = \frac{k_+}{k_-} \approx \exp\left(\frac{E_{\text{bind}}}{k_B T}\right) \tag{4.38}$$

where $E_{\text{bind}}$ is the binding energy and $k_B T \approx 25$ meV at room temperature. The fractional concentration in solution of a molecular species $X$ may be calculated in terms of the ratio of its mass $m$ in solution to its molar mass $\mu$, so that

$$C_X = \frac{m_X / \mu_X}{\sum_Y m_Y / \mu_Y}, \tag{4.39}$$

where the summation is over $Y \in \{\text{CNT}, \text{PVA}, \text{Brij 78}\}$. However, in order to obtain the molar mass $\mu$ and number of sites $s$ of the SWCNTs in solution, we first need an estimate of the

SWCNTs' average length $\ell_0$. In (4.37) we have neglected the possible adsorption of the Brij 78 solvent (Brij) in solution, as it is reasonable to assume that its binding energy is negligible on the SWCNT, i.e., $E_{\text{bind}}[\text{Brij 78}] \gtrsim 0$ eV. This is due to both the hydrophobic nature of SWCNTs and the comparatively strong binding of $E_{\text{bind}} \sim 0.5$ eV obtained for both SWCNTs and PVA.

## 4.3 Comparison of Experimental and Theoretical Results

To start analyzing the comparison between experimental and theoretical results, we must establish the importance of the percolation threshold. In figure 4.10 we can see that the concentrations used results in a number of adsorbed SWCNTs greater than that required by the percolation threshold (horizontal solid line). If we use a concentration that results in a number of adsorbed carbon nanotubes less than the percolation threshold, then there will not be enough CNTs to form a path that generates conductivity in the system and therefore a conductive polymer will not be obtained.

The comparison between the results of model 3 in section 4.2 and the experimental results can be seen in figure 4.11. Here we can see that there is a good correlation between the experimental and theoretical results in both the parallel conductivity (colored geometric figures) and the perpendicular conductivity (empty geometric figures) under various concentrations. There are certain exceptions of points that are not highly correlated, but this is attributable to the fact that there is significant noise in the experimental results due to external factors. However, in general, model 3 establishes a good correlation with the experimental results obtained.

According to our model, the surface conductivity anisotropy $\sigma^{\text{ani}} \equiv \sigma^{\parallel}/\sigma^{\perp}$, from (4.33) and (4.35), is described by

$$\sigma_{\text{mod}}^{\text{ani}} = \frac{\pi^2}{2} \frac{\lambda^{1/2}}{7\lambda + 3} \frac{\lambda^3 - 1 + \lambda^3 \left(1 - \frac{\arctan \sqrt{\lambda^3 - 1}}{\sqrt{\lambda^3 - 1}}\right)}{\lambda^3 \frac{\arctan \sqrt{\lambda^3 - 1}}{\sqrt{\lambda^3 - 1}} - 1}. \tag{4.40}$$

In Fig. 4.12 we see the comparison between the experimental and theoretical anisotropy, which again exhibit a good correlation with a relatively low standard deviation. More importantly, we may use (4.40) to design a PVA/SWCNT CPC with a given anisotropy in its conductivity, as demonstrated in Fig. 4.12.
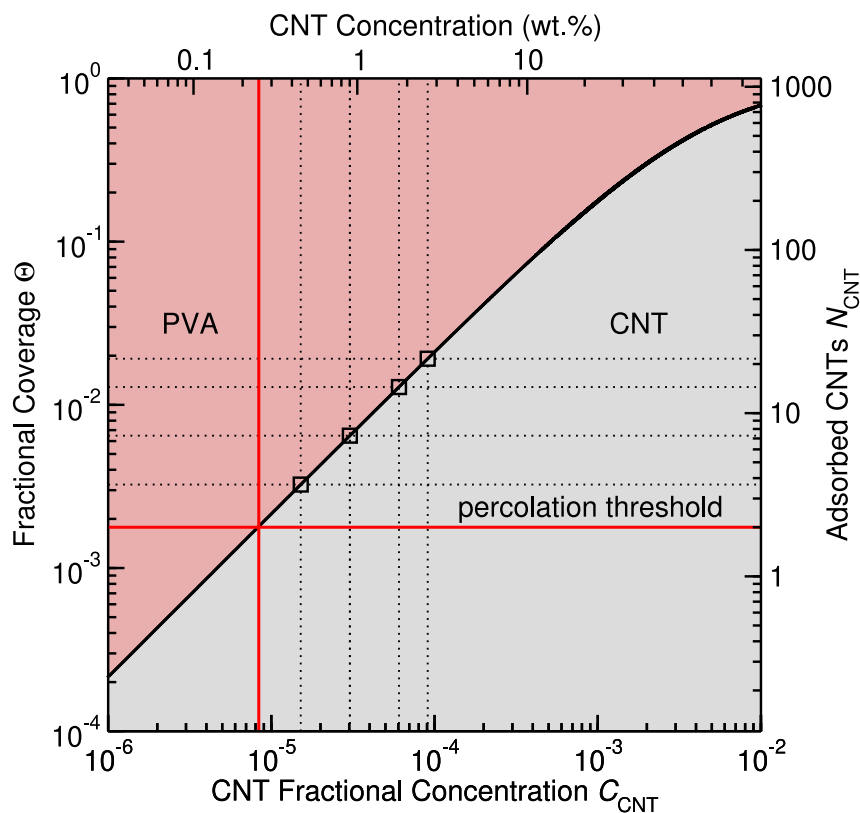
Figure 4.10:  Fractional coverage $\Theta$ of a SWCNT in solution by PVA (red region) or SWCNTs (grey region) and the number of adsorbed SWCNTs $N_{CNT}$ (black solid line) versus SWCNT fractional and weight % (wt.%) concentration $C_{CNT}$ in solution.  The threshold of two adsorbed SWCNTs per tube or $C_{CNT} \approx 0.25$ wt.% (red solid lines) for percolation is marked.  Results for the measured SWCNT concentrations of 0.45, 0.90, 1.79 and 2.65 wt.% are highlighted (black squares and dotted lines).

Finally, in Fig. 4.13 we can observe via a contour plot the results of model 3 and the experimental measurements.  These both depend on the extension ratio $\lambda$, concentration of SWCNTs $C_{CNT}$, the number of adsorbed SWCNTs $N_{CNT}$, and the orientational order parameter $S_g$.  As we can see, the conductivity parallel to the direction of stretching are identical, with the only difference that in model 3 a more fluid conductivity can be seen than in the experimental one.  Again, this is the most probably due to the experimental noises that affect the measurements.
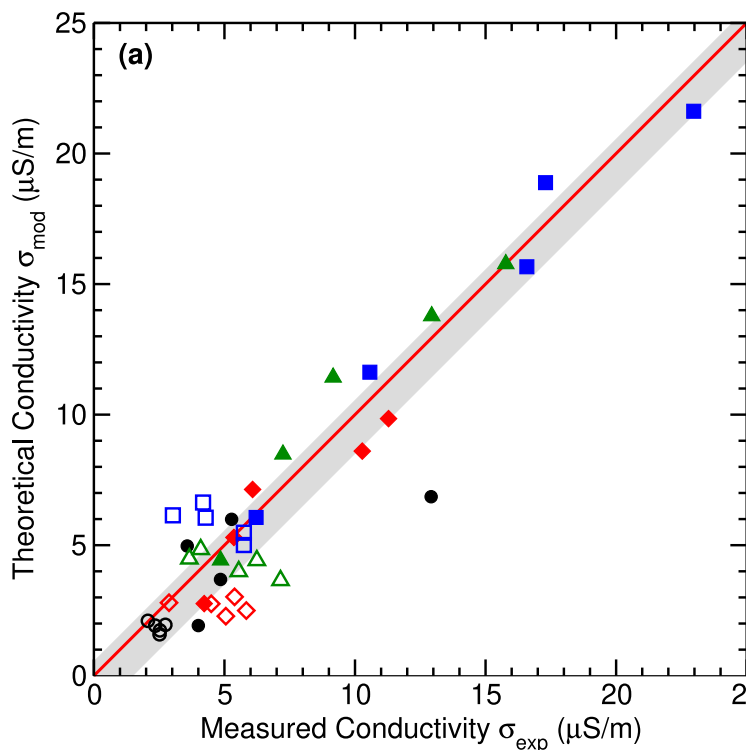
Figure 4.11: Conductivity of a PVA/CNT thin film from our theoretical model $\sigma_{mod}$ versus our experimental measurements $\sigma_{exp}$ in µS/m parallel (filled symbols) and perpendicular (open symbols) to the extension direction for extension ratios $\lambda = 1, 2, 3, 4, 5$ and SWCNT concentrations of 0.45 (black circles), 0.90 (red diamonds), 1.79 (green diamonds), and 2.65 (blue squares) wt.%, with an overall mean absolute error (MAE) of 1.4 µS/m and standard deviation of $\sigma \approx \pm 1.8$µS/m marked in grey.

and the number of measurements obtained. Similarly, for the perpendicular conductivity, we see that any differences observed between the experimental and theoretical conductance are within the observed noise in the measurement. Although a little more noise can be seen, they generally agree.
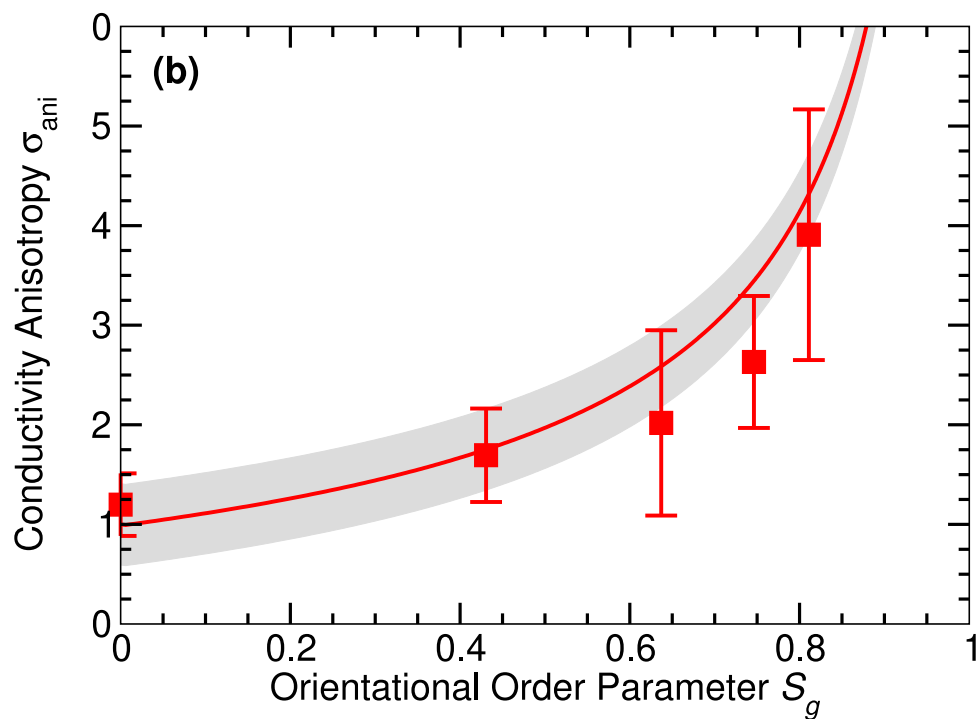
Figure 4.12: Conductivity anisotropy $\sigma_{\mathrm{ani}} \equiv \sigma^{\parallel}/\langle\sigma^{\perp}\rangle$ averaged over our experimental measurements (red squares) and from our model (4.40) (red solid line) with a standard deviation of $\sigma \approx \pm 0.408$ marked in grey.
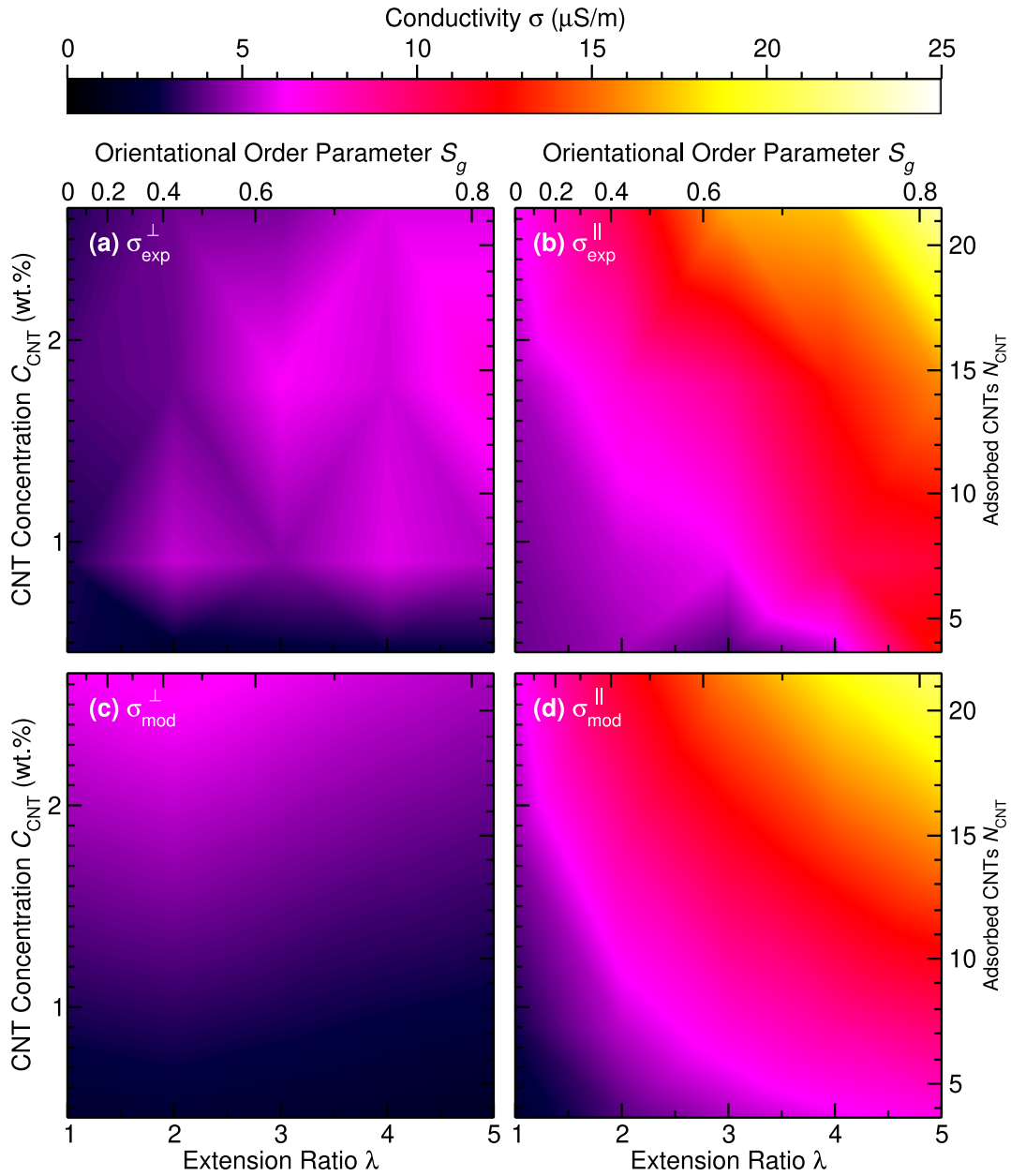
Figure 4.13: (a,b) Measured and (c,d) modelled conductivity $\sigma$ in μS/m (a,c) perpendicular and (b,d) parallel to the extension-direction versus SWCNT concentration $C_{CNT}$ in weight % (wt.%), number of adsorbed SWCNTs $N_{CNT}$, extension ratio $\lambda$ and orientational order parameter $S_g$ from (3.11).

# Chapter 5

# Conclusions & Outlook

In this thesis, we have established a general *ab initio* model to determine the conductivity of thin films of PVA/SWCNTs composites using DFT calculations and NEGF methods to establish a mathematical model that reproduces the experimental results both qualitatively and semi-quantitatively. Additionally, we propose a method to find the average length of SWCNTs in a TEM image in which no SWCNT can be fully seen in the image. This was done using a Monte Carlo approach and we expect that it gives a very close approximation to the average length of the carbon nanotubes in the sample. This in order that both established models can be extrapolated to systems under similar conditions and with slight changes in the materials used.

To begin with, from the characterization of the samples by means of Raman spectroscopy[91] in the RBM region, the predominant SWCNTs in each experimental phase were established through a deconvolution of the Raman spectrum. With this information, a comparison was made between the most abundant carbon nanotubes, which is the one that required the least computational capacity to simulate the conductance. Employing the PBE exchange and correlation functional and incorporating Van der Waals interactions via the Grimme's D3 correction for a better approximation to the experimental geometry, we then work on a mathematical model of the conductivity. While establishing the conductivity model, we had to develop a method to find the average length of a TEM image[103] of a sample treated in a similar (not equal) way to the thin film studied because no complete TEM image of the experimental sample studied was available. By means of Monte Carlo methods we deduced a close approximation to the average length of SWCNTs which turned

out to be a novel method to determine lengths in similar images.

Finally, we established the mathematical model and compared it with the experimental results through both contour plots and a direct comparison. We can clearly see that the model reproduces the experimental results, and forms a general model for CPCs containing ballistically conductive nanomaterials (SWCNTs) embedded in any polymeric matrix. The conductivity was calculated parallel and perpendicular to the stretching direction of the material and important parameters such as the orientation order and the concentration of SWCNTs in the sample were considered. We can conclude that this model shows that the CPCs conductivity is determined by (1) the connectivity of the SWCNT network within the polymer matrix, (2) the hopping resistance to intertube conductance, (3) the concentration of SWCNTs in the sample, and (4) the amount of stretching and concomitant orientational order parameter of the SWCNTs in the composite.

For future research, the models developed in this thesis can be applied to variations of the system conditions. For example, by changing the polymeric matrix and keeping single-walled carbon nanotubes or using multi-walled carbon nanotubes. Because the model generally describes the conductivity in conductive polymeric composites (CPCs), always considering that the nanomaterial that provides the electronic properties to the composite has ballistic conductivity. Finally, we encourage the academic community to develop similar experiments that adapt to the theoretical models to contrast and verify the final results.

# Appendix A

# Derivation of zenithal angle dependence

We begin from the equation of the geometric affine deformation model (3.6) to obtain the sine and cosine dependence of the final azimuthal angle $\theta$ in terms of the initial azimuthal angle $\theta_i$ as follows:

$$\tan \theta = \lambda^{-3/2} \tan \theta_i \tag{A.1}$$

$$\frac{\sin \theta}{\cos \theta} = \frac{\tan \theta_i}{\lambda^{3/2}}$$

$$\cos \theta = \frac{\lambda^{3/2}}{\tan \theta_i} \sin \theta$$

$$\cos^2 \theta = \frac{\lambda^3}{\tan^2 \theta_i} \sin^2 \theta$$

$$= \frac{\lambda^3}{\tan^2 \theta_i} (1 - \cos^2 \theta)$$

$$\cos^2 \theta \left( 1 + \frac{\lambda^3}{\tan^2 \theta_i} \right) = \frac{\lambda^3}{\tan^2 \theta_i}$$

$$\Rightarrow \cos^2 \theta = \frac{\lambda^3}{\lambda^3 + \tan^2 \theta_i} \tag{A.2}$$

$$1 - \sin^2 \theta = \frac{\lambda^3}{\lambda^3 + \tan^2 \theta_i}$$

$$\Rightarrow \sin^2 \theta = \frac{\tan^2 \theta_i}{\lambda^3 + \tan^2 \theta_i}. \tag{A.3}$$

69

Taking the square root of (A.2) and (A.3) we obtain

$$\cos\theta = \frac{\lambda^{3/2}}{\sqrt{\lambda^3 + \tan^2\theta_i}} \text{ and } \sin\theta = \frac{\tan\theta_i}{\sqrt{\lambda^3 + \tan^2\theta_i}}, \tag{A.4}$$

respectively.

## A.1   Average of Squared Cosine

To find the average value of the square of the cosine of the zenithal angle, we make the following derivation based on (A.2).

$$\langle\cos^2\theta\rangle = \int_0^{\frac{\pi}{2}} \frac{\lambda^3 \sin\theta_i d\theta_i}{\lambda^3 + \tan^2\theta_i} \tag{A.5}$$

$$= \int_0^{\frac{\pi}{2}} \frac{\lambda^3 \cos^2\theta_i \sin\theta_i}{\lambda^3 \cos^2\theta_i + \sin^2\theta_i} d\theta_i$$

$$= \int_0^{\frac{\pi}{2}} \frac{\lambda^3 \cos^2\theta_i \sin\theta_i}{(\lambda^3 - 1)\cos^2\theta_i + \cos^2\theta_i + \sin^2\theta_i} d\theta_i$$

$$= \int_0^{\frac{\pi}{2}} \frac{\lambda^3 \cos^2\theta_i \sin\theta_i}{(\lambda^3 - 1)\cos^2\theta_i + 1} d\theta_i$$

$$= \int_0^{\frac{\pi}{2}} \frac{\lambda^3 \cos^2\theta_i}{(\lambda^3 - 1)\cos^2\theta_i + 1} d(-\cos\theta_i)$$

$$= \int_{\frac{\pi}{2}}^0 \frac{\lambda^3 \cos^2\theta_i}{(\lambda^3 - 1)\cos^2\theta_i + 1} d(\cos\theta_i)$$

$$= \int_0^1 \frac{\lambda^3 y^2}{(\lambda^3 - 1)y^2 + 1} dy$$

$$= \frac{\lambda^3}{\lambda^3 - 1} \int_0^1 \frac{y^2}{y^2 + \frac{1}{\lambda^3 - 1}} dy$$

$$= \frac{\lambda^3}{\lambda^3 - 1} \left[ y - \frac{\arctan(y\sqrt{\lambda^3 - 1})}{\sqrt{\lambda^3 - 1}} \right]_0^1$$

$$\Rightarrow \langle\cos^2\theta\rangle = \frac{\lambda^3}{\lambda^3 - 1} \left( 1 - \frac{\arctan(\sqrt{\lambda^3 - 1})}{\sqrt{\lambda^3 - 1}} \right). \tag{A.6}$$

## A.2   Average of Squared Sine

To find the average of the square of the cosine of the zenithal angle, we make the following derivation based on (A.3).

$$\langle \sin^2 \theta \rangle = \int_0^{\frac{\pi}{2}} \frac{\tan^2 \theta_i \sin \theta_i d\theta_i}{\lambda^3 + \tan^2 \theta_i} \tag{A.7}$$

$$= \int_0^{\frac{\pi}{2}} \frac{\sin^3 \theta_i d\theta_i}{\lambda^3 \cos^2 \theta_i + \sin^2 \theta_i}$$

$$= \int_0^{\frac{\pi}{2}} \frac{1 - \cos^2 \theta_i}{(\lambda^3 - 1) \cos^2 \theta_i + 1} \sin \theta_i d\theta_i$$

$$= \int_0^1 \frac{1 - y^2}{(\lambda^3 - 1) y^2 + 1} dy$$

$$= \frac{1}{\lambda^3 - 1} \int_0^1 \frac{1 - y^2}{y^2 + \frac{1}{\lambda^3 - 1}} dy$$

$$= \frac{1}{\lambda^3 - 1} \left( \sqrt{\lambda^3 - 1} \arctan \sqrt{\lambda^3 - 1} - 1 + \frac{\arctan \sqrt{\lambda^3 - 1}}{\sqrt{\lambda^3 - 1}} \right)$$

$$= \frac{1}{\lambda^3 - 1} \left( \frac{\lambda^3 \arctan \sqrt{\lambda^3 - 1}}{\sqrt{\lambda^3 - 1}} - 1 \right)$$

$$\Rightarrow \langle \sin^2 \theta \rangle = \frac{\lambda^3}{\lambda^3 - 1} \left( \frac{\arctan \sqrt{\lambda^3 - 1}}{\sqrt{\lambda^3 - 1}} - \frac{1}{\lambda^3} \right). \tag{A.8}$$

## A.3   Average of Cosine

To find the average value of the cosine of the zenithal angle, we make the following derivation based on (A.4).

$$\langle \cos \theta \rangle = \int_0^{\frac{\pi}{2}} \frac{\lambda^{3/2} \sin \theta_i}{\sqrt{\lambda^3 + \tan^2 \theta_i}} d\theta_i \tag{A.9}$$

$$= \int_0^{\frac{\pi}{2}} \frac{\lambda^{3/2} \cos \theta_i \sin \theta_i}{\sqrt{\lambda^3 \cos^2 \theta_i + \sin^2 \theta_i}} d\theta_i$$

$$= \int_0^{\frac{\pi}{2}} \frac{\lambda^{3/2} \cos \theta_i}{\sqrt{(\lambda^3 - 1) \cos^2 \theta_i + 1}} d(-\cos \theta_i)$$

$$= \frac{\lambda^{3/2}}{\sqrt{\lambda^3 - 1}} \int_0^1 \frac{u}{\sqrt{u^2 + \frac{1}{\lambda^3 - 1}}} du$$

$$= \frac{\lambda^{3/2}}{\sqrt{\lambda^3 - 1}} \left( \sqrt{1 + \frac{1}{\lambda^3 - 1}} - \sqrt{\frac{1}{\lambda^3 - 1}} \right)$$

$$= \frac{\lambda^{3/2}}{\lambda^3 - 1} \left( \sqrt{\lambda^3 - 1 + 1} - 1 \right)$$

$$= \frac{\lambda^3}{\lambda^3 - 1} \left( 1 - \frac{1}{\lambda^{3/2}} \right),$$

$$= \frac{\lambda^{3/2}}{\lambda^{3/2} + 1} \frac{\lambda^{3/2} - 1}{\lambda^{3/2} - 1}$$

$$\Rightarrow \langle \cos \theta \rangle = \frac{\lambda^{3/2}}{\lambda^{3/2} + 1}. \tag{A.10}$$

## A.4   Average of Sine

To find the average value of the sine of the zenithal angle, we have resorted to an analytic estimate of the numerical result obtained based on (A.4).

$$\langle \sin \theta \rangle = \int_0^{\frac{\pi}{2}} \frac{\tan \theta_i \sin \theta_i}{\sqrt{\lambda^3 + \tan^2 \theta_i}} d\theta_i \tag{A.11}$$

$$= \int_0^{\frac{\pi}{2}} \frac{\sin^2 \theta_i}{\sqrt{\lambda^3 \cos^2 \theta_i + \sin^2 \theta_i}} d\theta_i$$

$$= \int_0^{\frac{\pi}{2}} \frac{\sin \theta_i}{\sqrt{\lambda^3 + (1 - \lambda^3) \sin^2 \theta_i}} d(-\cos \theta_i)$$

$$= \int_0^{\frac{\pi}{2}} \frac{\sin \theta_i}{\sqrt{(\lambda^3 - 1) \cos^2 \theta_i + 1}} d(-\cos \theta_i)$$

$$= \int_0^{\frac{\pi}{2}} \frac{\sqrt{1 - \cos^2 \theta_i}}{\sqrt{(\lambda^3 - 1) \cos^2 \theta_i + 1}} d(-\cos \theta_i)$$

$$= \int_0^1 \sqrt{\frac{1 - u^2}{(\lambda^3 - 1)u^2 + 1}} du$$

$$\Rightarrow \langle \sin \theta \rangle \approx \frac{1}{2} \frac{\sqrt{7\lambda + 3}}{\lambda^{3/2} + 1} \tag{A.12}$$

# Bibliography

[1] Lee, S. L.; Chang, C.-J. Recent Developments about Conductive Polymer Based Composite Photocatalysts. *Polymers* **2019**, *11*.

[2] Iijima, S. Helical microtubules of graphitic carbon. *Nature* **1991**, *354*, 56–58.

[3] Saito, R.; Dresselhaus, M.; Dresselhaus, G. *Physical Properties of Carbon Nanotubes*; Imperial College Press, 2005; pp 59–70.

[4] Dresselhaus, M. S.; Avouris, P.; Dresselhaus, M. S.; Dresselhaus, G.; Avouris, P. *Carbon Nanotubes: Synthesis, Structure, Properties, and Applications*, 1st ed.; Springer, 2001.

[5] Choi, W. B.; Chu, J. U.; Jeong, K. S.; Bae, E. J.; Lee, J.-W. Ultrahigh-density nanotransistors by using selectively grown vertical carbon nanotubes. *Appl. Phys. Lett.* **2001**, *79*, 3696.

[6] Tony McNally, P. P. *Polymer Carbon Nanotube Composites: Preparation, Properties and Applications*; Woodhead Publishing, 2011.

[7] Li, C.; Chou, T.-W. A structural mechanics approach for the analysis of carbon nanotubes. *International Journal of Solids and Structures* **2003**, *40*, 2487–2499.

[8] Chen, J.; Yan, L.; Song, W.; Xu, D. Interfacial characteristics of carbon nanotube-polymer composites: A review. *Composites Part A: Applied Science and Manufacturing* **2018**, *114*, 149–169.

[9] Yang, X.; Wang, J.; Guo, H.; Liu, L.; Xu, W.; Duan, G. Structural design toward functional materials by electrospinning: A review. *e-Polymers* **2020**, *20*, 682–712.

[10] Hwang, S.-H.; Park, Y.-B.; Han, K.; Suk, D. In *Carbon Nanotubes - Synthesis, Characterization, Applications*; Yellampalli, S., Ed.; InTech, 2011.

[11] Sahoo, N. G.; Rana, S.; Cho, J. W.; Li, L.; Chan, S. H. Polymer Nanocomposites Based on Functionalized Carbon Nanotubes. *Progress in Polymer Science* **2010**, *35*, 837–867.

[12] Luo, X.; Yang, G.; Schubert, D. W. Electrically Conductive Polymer Composite Containing Hybrid Graphene Nanoplatelets and Carbon Nanotubes: Synergistic Effect and Tunable Conductivity Anisotropy. *Adv Compos Hybrid Mater* **2022**, *5*, 250–262.

[13] Wang, J.; Jiang, C.; Li, W.; Xiao, X. Anisotropic Low-Dimensional Materials for Polarization-Sensitive Photodetectors: From Materials to Devices. *Advanced Optical Materials* **2022**, *10*, 2102436.

[14] Zamora-Ledezma, C.; Blanc, C.; Puech, N.; Maugey, M.; Zakri, C.; Anglaret, E.; Poulin, P. Conductivity Anisotropy of Assembled and Oriented Carbon Nanotubes. *Phys. Rev. E* **2011**, *84*, 062701.

[15] Zamora-Ledezma, C.; Blanc, C.; Anglaret, E. Controlled Alignment of Individual Single-Wall Carbon Nanotubes at High Concentrations in Polymer Matrices. *J. Phys. Chem. C* **2012**, *116*, 13760–13766.

[16] Yu, W.; Zhao, X.; Jiang, P.; Liu, C.; Yang, R. Tunable Anisotropic Thermal Transport in Super-Aligned Carbon Nanotube Films. *Materials Today Physics* **2021**, *20*, 100447.

[17] Chang, E.; Ameli, A.; Alian, A. R.; Mark, L. H.; Yu, K.; Wang, S.; Park, C. B. Percolation Mechanism and Effective Conductivity of Mechanically Deformed 3-Dimensional Composite Networks: Computational Modeling and Experimental Verification. *Composites Part B: Engineering* **2021**, *207*, 108552.

[18] Wang, Y.; Weng, G. J. In *Micromechanics and Nanomechanics of Composite Solids*; Meguid, S. A., Weng, G. J., Eds.; Springer International Publishing: Cham, 2018; pp 123–156.

[19] Li, L.; Shi, H.; Liu, Z.; Mi, L.; Zheng, G.; Liu, C.; Dai, K.; Shen, C. Anisotropic Conductive Polymer Composites Based on High Density Polyethylene/Carbon Nanotube/Polyoxyethylene Mixtures for Microcircuits Interconnection and Organic Vapor Sensor. *ACS Appl. Nano Mater.* **2019**, *2*, 3636–3647.

[20] Bai, J. B.; Allaoui, A. Effect of the Length and the Aggregate Size of MWNTs on the Improvement Efficiency of the Mechanical and Electrical Properties of Nanocomposites—Experimental Investigation. *Composites Part A: Applied Science and Manufacturing* **2003**, *34*, 689–694.

[21] Moeini, A.; Germann, N.; Malinconico, M.; Santagata, G. Formulation of secondary compounds as additives of biopolymer-based food packaging: A review. *Trends in Food Science & Technology* **2021**, *114*, 342–354.

[22] Mredha, M. T. I.; Jeon, I. Biomimetic Anisotropic Hydrogels: Advanced Fabrication Strategies, Extraordinary Functionalities, and Broad Applications. *Progress in Materials Science* **2022**, *124*, 100870.

[23] Han, J.; Xiong, L.; Jiang, X.; Yuan, X.; Zhao, Y.; Yang, D. Bio-Functional Electrospun Nanomaterials: From Topology Design to Biological Applications. *Progress in Polymer Science* **2019**, *91*, 1–28.

[24] Chang, J.-C.; Fujita, S.; Tonami, H.; Kato, K.; Iwata, H.; hui Hsu, S. Cell orientation and regulation of cell–cell communication in human mesenchymal stem cells on different patterns of electrospun fibers. *Biomedical Materials* **2013**, *8*, 055002.

[25] Mowbray, D. J.; Morgan, C.; Thygesen, K. S. Influence of O 2 and N 2 on the Conductivity of Carbon Nanotube Networks. *Phys. Rev. B* **2009**, *79*, 195431.

[26] Zhao, J.; Ma, D.; Wang, C.; Guo, Z.; Zhang, B.; Li, J.; Nie, G.; Xie, N.; Zhang, H. Recent advances in anisotropic two-dimensional materials and device applications. *Nano Research* **2021**, *14*, 897–919.

[27] Mutlay, I.; Tudoran, L. B. Percolation Behavior of Electrically Conductive Graphene Nanoplatelets/Polymer Nanocomposites: Theory and Experiment. *Fullerenes, Nanotubes and Carbon Nanostructures* **2014**, *22*, 413–433.

[28] Zhao, W.; Hu, S.; Shi, Z.; Santaniello, T.; Lenardi, C.; Huang, J. Mechanical Characteristics of Tunable Uniaxial Aligned Carbon Nanotubes Induced by Robotic Extrusion Technique for Hydrogel Nanocomposite. *Composites Part A: Applied Science and Manufacturing* **2020**, *129*, 105707.

[29] Fischer, J. E.; Zhou, W.; Vavro, J.; Llaguno, M. C.; Guthy, C.; Haggenmueller, R.; Casavant, M. J.; Walters, D. E.; Smalley, R. E. Magnetically aligned single wall carbon nanotube films: Preferred orientation and anisotropic transport properties. *Journal of Applied Physics* **2003**, *93*, 2157–2163.

[30] Gong, S.; Zhu, Z. H.; Meguid, S. A. Anisotropic Electrical Conductivity of Polymer Composites with Aligned Carbon Nanotubes. *Polymer* **2015**, *56*, 498–506.

[31] Ebbesen, T. W.; Lezec, H. J.; Hiura, H.; Bennett, J. W.; Ghaemi, H. F.; Thio, T. Electrical Conductivity of Individual Carbon Nanotubes. *Nature* **1996**, *382*, 54–56.

[32] Ma, P.-C.; Liu, M.-Y.; Zhang, H.; Wang, S.-Q.; Wang, R.; Wang, K.; Wong, Y.-K.; Tang, B.-Z.; Hong, S.-H.; Paik, K.-W.; Kim, J.-K. Enhanced Electrical Conductivity of Nanocomposites Containing Hybrid Fillers of Carbon Nanotubes and Carbon Black. *ACS Appl. Mater. Interfaces* **2009**, *1*, 1090–1096.

[33] Nørskov, J.; Bligaard, T.; Rossmeisl, J.; Christensen, C. Towards the computational design of solid catalysts. *Nature chemistry* **2009**, *1*, 37–46.

[34] Jain, A.; Ong, S.; Hautier, G.; Chen, W.; Richards, W.; Dacek, S.; Cholia, S.; Gunter, D.; Skinner, D.; Ceder, G.; Persson, K. Commentary: The Materials Project: A materials genome approach to accelerating materials innovation. *APL Materials* **2013**, *1*, 011002.

[35] Schrödinger, E. An Undulatory Theory of the Mechanics of Atoms and Molecules. *Physical Review* **1926**, *28*, 1049–1070.

[36] Haynes, P. Linear-scaling methods in ab initio quantum-mechanical calculations. Ph.D. Thesis, University of Cambridgee, 1998.

[37] Born, M.; Oppenheimer, R. Zur Quantentheorie der Molekeln. *Annalen der Physik* **1927**, *389*, 457.

[38] Kittel, C. *Introduction to Solid State Physics*, 7th ed.; 1996.

[39] Monkhorst, H. J.; Pack, J. D. Special points for Brillouin-zone integrations. *Physical Review B* **1976**, *13*, 5188–5192.

[40] Chadi, D. J.; Cohen, M. L. Efficient generation of generalized Monkhorst-Pack grids through the use of informatics. *Physical Review B* **1973**, *8*, 5747–5753.

[41] Wisesa, P.; McGill, K. A.; Mueller, T. Special Points in the Brillouin Zone. *Physical Review B* **2016**, *93*.

[42] Hohenberg, P.; Kohn, W. Inhomogeneous Electron Gas. *Physical Review* **1964**, *136*, B864–B871.

[43] Engel, E.; Dreizler, R. M. *Density Functional Theory: An Advanced Course*, 1st ed.; Theoretical and Mathematical Physics (United States); Springer, 2011.

[44] Kohn, W.; Sham, L. J. Self-Consistent Equations Including Exchange and Correlation Effects. *Physical Review* **1965**, *140*, A1133–A1138.

[45] Hartree, D. R. The Wave Mechanics of an Atom with a Non-Coulomb Central Field. Part I. Theory and Methods. Ph.D. Thesis, University of Cambridgee, 1928.

[46] Feynman, R. P. Forces in Molecules. *Physical Review* **1939**, *56*, 340–343.

[47] Sholl, D.; Steckel, J. A. *Density functional theory: A practical introduction*; Wiley-Interscience, 2009.

[48] Becke, A. D. Perspective: Fifty years of density-functional theory in chemical physics. *The Journal of Chemical Physics* **2014**, *140*, 18A301.

[49] Perdew, J. P.; Burke, K.; Ernzerhof, M. Generalized Gradient Approximation Made Simple. *Physical Review Letters* **1996**, *77*, 3865–3868.

[50] Perdew, J. P.; Ruzsinszky, A.; Csonka, G. I.; Vydrov, O. A.; Scuseria, G. E.; Constantin, L. A.; Zhou, X.; Burke, K. Restoring the Density-Gradient Expansion for Exchange in Solids and Surfaces. *Physical Review Letters* **2008**, *100*.

[51] Perdew, J. P.; Ernzerhof, M.; Zupan, A.; Burke, K. Distributions and averages of electron density parameters: Explaining the effects of gradient corrections. *The Journal of Chemical Physics* **1998**, *106*, 10184–10193.

[52] Perdew, J. P.; Ruzsinszky, A.; Csonka, G. I.; Vydrov, O. A.; Scuseria, G. E.; Constantin, L. A.; Zhou, X.; Burke, K. Restoring the Density-Gradient Expansion for Exchange in Solids and Surfaces. *Physical Review Letters* **1998**, *108*, 1522–1531.

[53] Grimme, S.; Antony, J.; Ehrlich, S.; Krieg, H. A consistent and accurate ab initio parametrization of density functional dispersion correction (DFT-D) for the 94 elements H-Pu. *The Journal of chemical physics* **2010**, *132 15*, 154104.

[54] Chelikowsky, J. R.; Troullier, N.; Saad, Y. Finite-difference-pseudopotential method: Electronic structure calculations without a basis. *Physical Review Letters* **1994**, *72*, 1240–1243.

[55] Heiskanen, M.; Torsti, T.; Puska, R. M., M. J.and Nieminen Multigrid method for electronic structure calculations. *Physical Review B* **2001**, *63*.

[56] Grossmann, C.; Roos, H.-G.; Stynes, M. *Numerical treatment of partial differential equations*, 1st ed.; Universitext; Springer, 2007.

[57] Clark, T.; Koch, R. *The Chemist's Electronic Book of Orbitals*, 1st ed.; Springer, 1999; pp 5–22.

[58] Artacho, E.; Anglada, E.; Diéguez, O.; Gale, J. D.; García, A.; Junquera, J.; Martin, R. M.; Ordejón, P.; Pruneda, J. M.; Sánchez-Portal, D.; Soler, J. M. The SIESTA method; developments and applicability. *Journal of Physics: Condensed Matter* **2008**, *20*, 64208.

[59] Larsen, A. H.; Vanin, M.; Mortensen, J. J.; Thygesen, K. S.; Jacobsen, K. W. Localized Atomic Basis Set in the Projector Augmented Wave Method. *Physical Review B* **2009**, *80*, 195112.

[60] Sankey, O. F.; Niklewski, D. J. Ab initio multicenter tight-binding model for moleculardynamics simulations and other applications in covalent systems. *Physical Review B* **1989**, *40*, 3979.

[61] Anglada, E. M.; Soler, J.; Junquera, J.; Artacho, E. Systematic generation of finite-range atomic basis sets for linear-scaling calculations. *Physical Review B* **2002**, *66*, 205101.

[62] Larsen, A. H. Localized atomic basis set in the projector augmented wave method. *Physical Review B* **2008**, *80*.

[63] Vanin, M. Projector Augmented Wave Calculations with Localized Atomic Orbitals. Ph.D. Thesis, Technical University of Denmark, 2008.

[64] Soler, J. M.; Artacho, E.; Gale, J. D.; Garcia, A.; Junquera, J.; Ordejón, P.; Sánchez-Portal, D. The SIESTA method for ab initio order-N materials simulation. *Journal of Physics: Condensed Matter* **2002**, *14*, 2745.

[65] Haydock, R.; Heine, V.; Kelly, M. J. Electronic structure based on the local atomic environment for tight-binding bands. II. *Journal of Physics C: Solid State Physics* **1975**, *8*, 2591–2605.

[66] Pickett, W. E. Pseudopotential methods in condensed matter applications. *Computer Physics Report* **1989**, *9*, 115–197.

[67] Slater, J. C. An Augmented Plane Wave Method for the Periodic Potential Problem. *Physical Review* **1953**, *92*, 603–608.

[68] Blöchl, P. E. Projector augmented-wave method. *Physical Review B* **1994**, *50*, 17953–17979.

[69] Mortensen, J. J.; Hansen, L. B.; Jacobsen, K. W. Real-space grid implementation of the projector augmented wave method. *Physical Review B* **2005**, *71*.

[70] Agraıt, N.; Yeyati, A. L.; Van Ruitenbeek, J. M. Quantum properties of atomic-sized conductors. *Springer Science & Business Media* **2003**, *377*, 87–279.

[71] Nitzan, A.; Ratner, M. A. Electron transport in molecular wire junctions. *Science* **2003**, *300*, 1384–1389.

[72] Kurth, S.; Perdew, J. P.; Blaha, P. Molecular and solid-state tests of density functional approximations: LSD, GGAs, and meta-GGAs. *Int. Journal of Quantum Chemistry* **1999**, *75*, 889–909.

[73] Landauer, R. Spatial variation of currents and fields due to localized scatterers in metallic conduction. *Int. Journal of Quantum Chemistry* **1957**, *1*, 223–231.

[74] Landauer, R. Electrical resistance of disordered one-dimensional lattices. *Philosophical Magazine* **1970**, *21*, 863–867.

[75] Büttiker, M. Four-Terminal Phase-Coherent Conductance. *Physical Review Letters* **1986**, *57*, 1761–1764.

[76] Meir, Y.; Wingreen, N. S. Landauer formula for the current through an interacting electron region. *Physical Review Letters* **1992**, *68*, 2512.

[77] Guinea, F.; Tejedor, C.; Flores, F.; Louis, E. Effective two-dimensional Hamiltonian at surfaces. *Physical Review B* **1983**, *28*, 4397.

[78] Dyson, F. J. The *S* Matrix in Quantum Electrodynamics. *Physical Review* **1949**, *75*, 1736–1755.

[79] Strange, M.; Kristensen, I. S.; Thygesen, K. S.; Jacobsen, K. W. Benchmark density functional theory calculations for nanoscale conductance. *The Journal of Chemical Physics* **2008**, *128*, 114714.

[80] Brandbyge, M.; Mozos, J.-L.; Ordejón, P.; Taylor, J.; Stokbro, K. Density-functional method for nonequilibrium electron transport. *Physical Review B* **2002**, *65*, 165401.

[81] Larsen, A. J.; Mortensen, J. J.; Blomqvist, J.; Castelli, I. E.; Christensen, R.; Duak, M.; Jacobsen, K. W. The atomic simulation environment—a Python library for working with atoms. *Journal of Physics: Condensed Matter* **2017**, *29*, 273002.

[82] Mortensen, J. J.; Hansen, L. B.; Jacobsen, K. W. Real-space grid implementation of the projector augmented wave method. *Physical Review B* **2005**, *71*, 35109.

[83] Yoshizawa, K.; Tada, T.; Staykov, A. Orbital views of the electron transport in molecular devices. *Journal of the American Chemical Society* **2008**, *130*, 9406–9413.

[84] Jensen, A.; Garner, M. H.; Solomon, G. C. When Current Does Not Follow Bonds: Current Density in Saturated Molecules. *Journal of Chemical Physics C* **2019**, *123*, 12042–12051.

[85] Delaney, P.; Greer, J. C. Correlated electron transport in molecular electronics. *Physical Review Letters* **2004**, *93*, 36805.

[86] Varga, K. Time-dependent density functional study of transport in molecular junctions. *Physical Review B* **2011**, *83*, 195130.

[87] Grimmett, G. *Percolation*; Springer, 1989.

[88] Landau, R. H.; Mejía, M. J. P. *Computational Physics: Problem Solving With Computers*, har/dis/co ed.; Wiley-Interscience, 1997.

[89] Saito, R.; Dresselhaus, G.; Dresselhaus, M. S. *Physical properties of carbon nanotubes*, 1st ed.; World Scientific Publishing Company, 1998.

[90] Lu, X.; Chen, Z. Curved Pi-Conjugation, Aromaticity, and the Related Chemistry of Small Fullerenes (¡C60) and Single-Walled Carbon Nanotubes. *ChemInform* **2006**, *37*.

[91] Fernández, J. S. Caracterización óptica y eléctrica de compuestos orgánicos anisotrópicos basados en nanotubos de carbono. diploma thesis, Departamento de Física, 2013.

[92] Zamora-Ledezma, C.; Mowbray, D.; Machaé, J.; Suárez, J. L.; Bramer, W. developing.

[93] Bahn, S. R.; Jacobsen, K. W. An Object-Oriented Scripting Interface to a Legacy Electronic Structure Code. *Comput. Sci. Eng.* **2002**, *4*, 56.

[94] Mortensen, J. J.; Hansen, L. B.; Jacobsen, K. W. Real-Space Grid Implementation of the Projector Augmented Wave Method. *Phys. Rev. B* **2005**, *71*, 035109.

[95] Enkovaara, J. *et al.* Electronic Structure Calculations with GPAW: A Real-Space Implementation of the Projector Augmented-Wave Method. *J. Phys.: Condens. Matter* **2010**, *22*, 253202.

[96] Maultzsch, J.; Telg, H.; Reich, S.; Thomsen, C. Radial Breathing Mode of Single-Walled Carbon Nanotubes: Optical Transition Energies and Chiral-Index Assignment. *Phys. Rev. B* **2005**, *72*, 205438.

[97] Rols, S.; Righi, A.; Alvarez, L.; Anglaret, E.; Almairac, R.; Journet, C.; Bernier, P.; Sauvajol, J. L.; Benito, A. M.; Maser, W. K.; Muñoz, E.; Martinez, M. T.; de laFuente, G. F.; Girard, A.; Ameline, J. C. Diameter Distribution of Single Wall Carbon Nanotubes in Nanobundles. *Eur. Phys. J. B* **2000**, *18*, 201–205.

[98] Narváez-Muñoz, C.; Diaz-Suntaxi, D. F.; Carrión-Matamoros, L. M.; Guerrero, V. H.; Almeida-Naranjo, C. E.; Morales-Flórez, V.; Debut, A.; Vizuete, K.; Mowbray, D. J.; Zamora-Ledezma, C. Impact of the solvent composition on the structural and mechanical properties of customizable electrospun poly(vinylpyrrolidone) fiber mats. *Phys. Chem. Chem. Phys.* **2021**, *23*, 22923–22935.

[99] Zhbanov, A.; Pogorelov, E.; Chang, Y. Van der Waals Interaction between Two Crossed Carbon Nanotubes. *ACS nano* **2010**, *4*, 5937–45.

[100] Zamora-Ledezma, C.; Blanc, C.; Anglaret, E. Orientational order of single-wall carbon nanotubes in stretch-aligned photoluminescent composite films. *Phys. Rev. B* **2009**, *80*, 113407.

[101] Ahir, S. V.; Squires, A. M.; Tajbakhsh, A. R.; Terentjev, E. M. Infrared Actuation in Aligned Polymer-Nanotube Composites. *Phys. Rev. B* **2006**, *73*, 085420.

[102] Cañas, F. J. T. Tintas y Materiales Compuestos Anisotrópicos Basados en Nanotubos de Carbono. Ph.D. thesis, Instituto Venezolano de Investigaciones Científicas, 2015.

[103] Puech, N.; Blanc, C.; Grelet, E.; Zamora-Ledezma, C.; Maugey, M.; Zakri, C.; Anglaret, E.; Poulin, P. Highly Ordered Carbon Nanotube Nematic Liquid Crystals. *The Journal of Physical Chemistry C* **2011**, *115*, 3272–3278.